

August 29, 2014

BACHELOR ASSIGNMENT

ROTATING A GOLD NANOROD USING OPTICALLY IN- DUCED TORQUE



Nico Hendrickx
s1229559
Kit de Hond
s1237896

Tutor: Dr. E.S. Kooij

Faculty of Science and Technology
Physics of Interfaces and Nanomaterials

UNIVERSITY OF TWENTE.

Summary

In this thesis the possible torque on a gold nanoparticle with an aspect ratio of 7 is investigated using the discrete dipole approximation (DDA). For the different plasmon resonance modes the extinction and torque spectra are computed and the electric field is visualised together with the charge distribution. We found that the torque is at a maximum for particles oriented at 45° relative to the polarization and k-vector of the incident light. Furthermore the dipole resonance rendered the largest torque. For a particle with a short radius of 19 nm this maximum torque was determined to be 1.15×10^{-18} Nm. This torque is compared to the Brownian motion and it was found that the rotational energy associated with this torque is not enough to overcome the Brownian motion. However, experimental results show that for a similar torque alignment may be possible. This suggests there might be invalidities in the energy analysis used in this report.

The dipole and octupole modes behave as expected, since a change in the charge distribution was observed causing the torque to oscillate. However, the quadrupole exhibits a static charge distribution, contradicting the torque oscillation that was visible in the quadrupole torque spectrum. A fitting explanation for this phenomenon is not yet found.

Contents

Summary	i
1 Introduction	1
2 Theory	3
2.1 Localized surface plasmon resonance	3
2.1.1 Torque induced by LSPR	4
2.2 Discrete dipole approximation	5
3 Methods	7
3.1 DDSCAT	7
3.1.1 Configuring the parameter file	7
3.1.2 Laboratory and target frame	8
3.1.3 Accuracy	9
3.1.4 Near field calculations	10
3.2 Processing with Matlab	10
4 Results & Discussion	13
4.1 Extinction and torque spectra	13
4.1.1 Dipole	15
4.1.2 Quadrupole	16
4.1.3 Octupole	17
4.1.4 Possible torque	17
4.2 Charge distribution	18
4.2.1 Dipole	18
4.2.2 Quadrupole	22
4.2.3 Octupole	25
4.3 Improvements and recommendations	28
5 Conclusion	29
6 Acknowledgements	31
A Effective radius	35
B Macroscopic vs. microscopic field	36
C Angle dependence of torque	37
D Example Parameter file	38
E Fortran code added to ddpostprocess.f90	39
F Importing data	41
G Processing the fields	43

Chapter 1

Introduction

Surface plasmon resonances (SPR) have been a research subject for many years. When a metallic particle is exposed to an incident light beam this may give rise to collective excitation of electrons [1]. Surface plasmon resonances result in a peak in the extinction spectra of the investigated particles. The position of this peak is determined by the shape, size and material of the particle. When considering metallic ellipsoidal particles, different peaks can be observed corresponding to different resonance modes. For example, a prolate spheroidal particle clearly exhibits two peaks in its extinction spectrum: one from the transverse mode and another one from the longitudinal resonance mode. For larger particles it is also possible to excite higher order resonances such as the quadrupole and octupole modes. If the particle has dimensions in the nanometer range, so that its dimensions are significantly smaller than the wavelength of the incident light, SPR is referred to as localized surface plasmon resonance or LSPR. When considering LSPR, the dipole mode usually is the most significant. Therefore the particle exhibits very similar behaviour to an electric dipole.

A dipole in an electric field can experience a torque when exposed to linearly polarized radiation [2]. Therefore an anisotropic particle located in an electric field may also experience a torque due to its similarity to a dipole. Several studies have been conducted to find out how large this torque on a metallic nanoparticle can be and if it would be possible to align anisotropic particles with the polarization direction of the incident wave [3]. In order to do so, the torque that acts upon the particles has to be large enough to overcome Brownian motion. These studies have obtained torques varying between 10×10^{-11} Nm and 10×10^{-19} Nm [3–6]

For particles exhibiting certain symmetries, spherical or cylindrical for example, Mie theory is an analytical method to solve Maxwell's equations and thereby provides us with the means to calculate the electric field [7]. However, when dealing with differently shaped particles Mie theory no longer suffices and numerical methods have to be used. A frequently used method to determine the properties of anisotropic nanoparticles is the discrete dipole approximation (DDA) [1, 8, 9]. The DDA approaches a particle as a collection of a large number of dipoles enabling the user to numerically solve a variety of problems. For instance, the DDA has been used to calculate extinction spectra of noble metal nanoparticles among other properties [1, 8].

In this thesis the DDA will be used in order to study the torque on gold, anisotropic nanoparticles. The wide range of published torque values suggests that there is no consensus yet. Using the DDA an attempt is made to find a conclusive answer for this problem. Furthermore, these torque values will be used to investigate if it is possible to overcome Brownian rotation. Also, the electric field near the particle is visualized in order to understand the underlying principles causing the particle to rotate. This is done by simulating the electric field of particles with different effective radii and orientations for a broad spectrum of wavelengths. This way, the different modes (dipole, quadrupole etc.) will all be investigated.

Chapter 2

Theory

2.1 Localized surface plasmon resonance

When a metal particle is exposed to incident radiation, its electron cloud shifts opposite to the incident field as can be seen in figure 2.1. In case the frequency of the incoming wave matches the resonance frequency of the electrons, a surface plasmon resonance (SPR) is excited. If the particle is substantially smaller than the wavelength of the incident light, this phenomenon is referred to as localized surface plasmon resonance or LSPR.

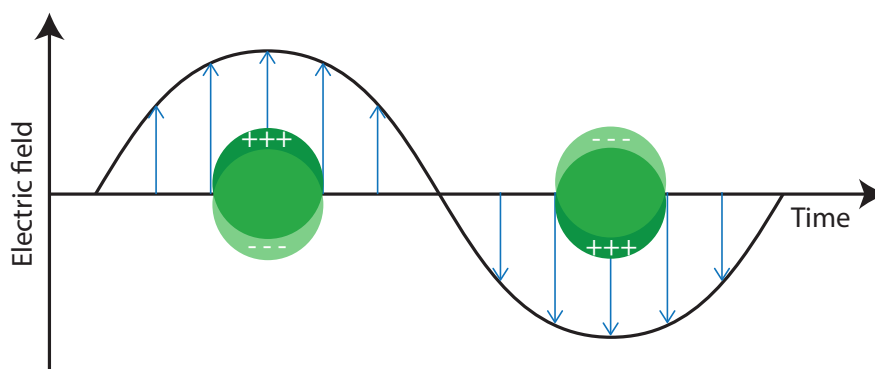


Figure 2.1: Schematic illustration of a light wave causing a localized surface plasmon resonance.

A commonly used method to analyse LSPR is to plot extinction spectra. In these spectra the extinction efficiency factor Q_{ext} is measured as a function of wavelength. The total extinction has two contributing factors: absorption and scattering. Q_{ext} is simply the sum of these two factors: $Q_{ext} = Q_{abs} + Q_{sca}$ [7].

In extinction spectra, an LSPR is clearly visible as a sharp peak at the plasmon resonance frequency. Since multiple modes can be excited (transverse, longitudinal) and these modes can have higher order resonances (quadrupole, octupole etc.), most extinction spectra exhibit multiple peaks. The shape of these peaks can be explained by looking at the polarizability of the particle: α . This α is a complex function with a phase lag ϕ with respect to the incident electric field. When the condition $\phi = \pi/2$ holds, it means that $Re(\alpha) = 0$. At that point, the imaginary part of α is at its maximum, which corresponds to the maximum absorption [5]. This can be verified for an upright prolate spheroid using the equation formulated by Gans [10]

$$\alpha \propto \frac{\epsilon_r(\omega) - 1}{1 + [\epsilon_r(\omega) - 1]L} \quad (2.1)$$

where α is the polarizability, $\epsilon_r(\omega)$ the relative permittivity of the particle and L the depolarization factor. L is related to the aspect ratios of the particle. For a sphere, L is equal to $1/3$, for a very prolate spheroid

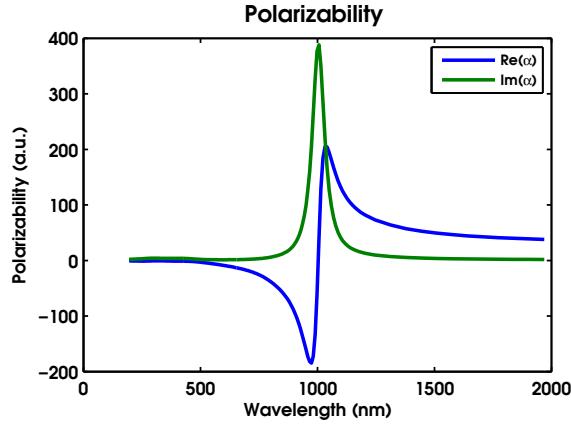


Figure 2.2: Real and imaginary part of the polarizability of an upright prolate spheroid with an aspect ratio of 7. This corresponds to an L of approximately 0.035 [11].

(i.e. a needle) L approaches 1 and for a very oblate particle (i.e. disk) L approaches 0. Using equation 2.1 a spectrum for α is plotted in figure 2.2. This type of oscillation is characteristic for a Lorentz oscillator.

Note that in order to see even modes the particle has to be oriented at an angle between 0° and 90° in the $E\mathbf{k}$ -plane. When the target is oriented at 0° or 90° the even modes are forbidden due to symmetry reasons [12–14].

The wavelength at which a certain mode will occur, will redshift for increasing particle size [1]. This can be explained by the fact that the wavelength of the incident light has to increase as well in order for a standing surface wave to fit on the particle. Another explanation for the redshift is that for a larger particle the opposite charges get separated further apart. This results in a smaller counterforce and therefore less energy is needed to excite the LSPR. That makes longer wavelengths suitable for exciting a resonance.

2.1.1 Torque induced by LSPR

Localized surface plasmon resonances cause a separation of charges in the particle. Because of this separation a net dipole moment occurs, which gives rise to a torque that can be calculated by:

$$\mathbf{\Gamma} = \mathbf{p} \times \mathbf{E} \quad (2.2)$$

Here $\mathbf{\Gamma}$ is the torque, \mathbf{p} is the dipole moment and \mathbf{E} is the electric field. The size of this torque largely depends on the polarizability of the target and the intensity of the incident field. When dealing with torques sometimes the torque efficiency vector is used, which is given by [15]:

$$\mathbf{Q}_\Gamma = \frac{k\mathbf{\Gamma}}{\pi a_{eff}^2 u_{rad}} \quad (2.3)$$

where \mathbf{Q}_Γ is the torque efficiency vector, k the wavenumber, a_{eff} the effective radius and u_{rad} the time-averaged energy density for an incident plane wave with amplitude $E_0 \cos(\omega t + \phi)$. u_{rad} is given by:

$$u_{rad} = \epsilon_m \frac{E_0^2}{8\pi} \quad (2.4)$$

where ϵ_m is the permittivity of the medium and E_0 is the amplitude of the electric field. This amplitude can be calculated from [2]:

$$E_0^2 = \frac{2I}{c\epsilon_m} \quad (2.5)$$

where I is the intensity and c the speed of light in vacuum.

Energy analysis

In order to compare the torque to other forces, such as the Brownian motion, one should calculate the

rotational energy of the particle. This can be done by considering a simple equation of motion for a particle in a fluid:

$$I \frac{d^2\theta}{dt^2} = \Gamma - \gamma \frac{d\theta}{dt} \quad (2.6)$$

I is the moment of inertia of the particle, θ the angle of rotation and γ is the rotational drag coefficient. The left hand side of the equation is simply the general inertia term and the right hand side consists of a term for the torque and one for the drag. The rotational drag coefficient is given by [16]:

$$\gamma = \frac{\pi\eta h^3}{3[\ln \frac{h}{2r} - 0.66]} \quad (2.7)$$

In this equation η is the viscosity of the fluid, h is the length of the particle and r is the short radius of the particle. If a stationary situation is considered, the left hand side of the equation of motion is equal to zero. Therefore it must hold that:

$$\omega = \frac{d\theta}{dt} = \frac{\Gamma}{\gamma} \quad (2.8)$$

where ω is the rotational velocity. The rotational energy of a system is given by:

$$E_{rot} = \frac{1}{2} I \omega^2 \quad (2.9)$$

In order to calculate this energy, the moment of inertia is needed. If a cylinder is considered, the moment of inertia can be calculated using the next equation:

$$I_{cyl} = \frac{1}{12} m [3r^2 + h^2] \quad (2.10)$$

where m is the total mass of the target.

Charge distribution

It can be useful to visualize the surface charge distribution on the target surface. This may be convenient to understand the origin of the torque. The charge distribution can be calculated from the electric field using the first Maxwell equation: Gauss's law [2].

$$\nabla \cdot \mathbf{E} = \frac{\rho}{\epsilon_0} \quad (2.11)$$

Here ρ is the charge density and ϵ_0 is the permittivity of free space.

In Gaussian units, this equation reads:

$$\nabla \cdot \mathbf{E} = 4\pi\rho \quad (2.12)$$

2.2 Discrete dipole approximation

The discrete dipole approximation, or DDA for short, is a numerical method for computing scattering and absorption of electromagnetic waves by targets with arbitrary geometries and complex refractive index. The target is approximated as an array of point dipoles. An iterative algorithm is used to obtain a numerical solution that satisfies Maxwell's equations for the system. FFT methods are used to reduce computational time when executing many large matrix multiplications. Using DDA, geometries that cannot be solved analytically, using Mie theory for example, can be analysed anyway [17].

Validity of the DDA

The DDA software uses both the microscopic and the macroscopic electric field, \mathbf{E}_{micro} and \mathbf{E}_{macro} respectively. The microscopic field is the field as it acts on a single dipole. The macroscopic field is the electric field as it is observed from outside the target. So to say, for the macroscopic field the target is regarded as a whole instead of a collection of many individual dipoles. Ordinarily when people talk about electric fields inside matter, they refer to the macroscopic field. The relation between the microscopic and macroscopic field follows from the Clausius-Mossotti relation (see Appendix B):

$$\mathbf{E}_{micro} = \left(\frac{\epsilon_r(\omega) + 2}{3} \right) \mathbf{E}_{macro} \quad (2.13)$$

where $\epsilon_r(\omega)$ is the relative permittivity of the target.

In order to check the validity of the DDA calculation one should check if the following relation holds:

$$\mathbf{P}_j = \boldsymbol{\alpha}_j \cdot \mathbf{E}_{j,micro} \quad (2.14)$$

Here $\boldsymbol{\alpha}$ is the diagonal polarizability tensor. The subscript j is an index for every dipole site. Since an exact solution would satisfy equation 2.14 [15] and this relation is not used in the DDA to calculate the polarization, it can be used to verify the numerical results given by the DDA.

Dipole moment

As the DDA approximates the target particle as an array of dipoles, it is possible to calculate the net dipole moment. This can be done in two different ways. The first is simply executing a summation over the polarization of all the point dipoles (equation 2.15). The second option is to calculate the charge at each point and multiply that by its position vector (equation 2.16). Note that the position of the origin does not matter since the total charge of the target is always zero [2].

$$\mathbf{p} = \sum_{i=1}^n \mathbf{p}_i = \sum_{i=1}^n \mathbf{P}_i d^3 \quad (2.15)$$

$$\mathbf{p} = \sum_{i=1}^n q_i \mathbf{r}_i = \sum_{i=1}^n \rho_i d^3 \mathbf{r}_i \quad (2.16)$$

Here the summation runs over every computational element, \mathbf{p} is the dipole moment, \mathbf{P} is the polarization, d is the dipole spacing, q is the charge and \mathbf{r} is the position vector.

Chapter 3

Methods

The program that will be used for this thesis is called DDSCAT. This software has been developed by Draine and Flatau and uses the DDA in order to calculate the optical properties of nanoparticles [17, 18]. The DDSCAT software is freely available and comes with a parameter file so the user can configure the software for his/her research purposes.

3.1 DDSCAT

DDSCAT is run in a Linux environment and is compiled using single precision, OpenMP and the Intel Math Kernel Library. The parameter file that comes with DDSCAT lets you specify all the variables needed for the simulation. An example can be found in appendix D.

3.1.1 Configuring the parameter file

The file starts with a few preliminaries. DDSCAT is capable of calculating the torque on a particle. However, since this is quite CPU consuming, one might choose not to use this option. Line 5 specifies the FFT method that is used. Since the Intel MKL is significantly faster, that method was used for this research. The other preliminaries were left unchanged. The values for GAMMA (line 23), ETASCA (line 25), NAMBIENT (line 29), IWRKSC (line 36) were also left at their default setting.

The shape of the particle can be set in line 11 and 12. DDSCAT supports many target geometries that can be found in the user guide. The shape parameters on line 12 lets the user select the amount of dipoles that should be used and also the aspect ratios. When choosing the number of dipoles the user should keep in mind that more dipoles results in more accurate results. However, the more dipoles are used, the longer it will take to do any calculations. The calculations in this thesis were done with approximately 15,000 to 20,000 dipoles. For this report the target geometry was the capped cylinder, which is a cylinder with two hemispheres on top of the ends. This geometry was chosen since it exhibits the most resemblance to a physical nanorod (figure 3.1). The standard orientation of the capped cylinder is as follows: cylinder axis = $\hat{a}_1 = (1, 0, 0)_{TF}$ and $\hat{a}_2 = (0, 1, 0)_{TF}$. Here the subscript TF indicate the directions are in the target frame, which will be explained in section 3.1.2.

Line 14 is used to set the dielectric function of the material that is investigated. In our case the dielectric function of gold in water as determined by E.D. Palik was used (figure 3.2 [20]). In order to use this file, the wavelengths for each simulation had to be converted from water to vacuum.

In the next few lines the options for the near field calculations can be set. These will be discussed later in this chapter. Line 19 specifies the error tolerance. The smaller this number, the more accurate the solution will be, but this will also increase the amount of iterations needed. The maximum amount of iterations before the software stops is set in line 21. This number was set at 10,000 because some problems took more than 1,000 iterations to converge.

The settings for wavelengths, effective radii and target rotations determine for which situations the calculations are run. Again, note that the dielectric function that was used represented gold in water so all wavelengths were converted. The incident polarization was left in its original direction, which is polarization in the y-direction of the lab frame.

All other options can be used to set up the calculation of Mueller matrix elements. Since this matrix was irrelevant for this research we will not elaborate on this further.

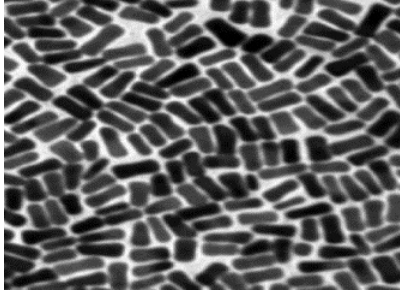


Figure 3.1: TEM image of a dense ensemble of gold nanorods [19].

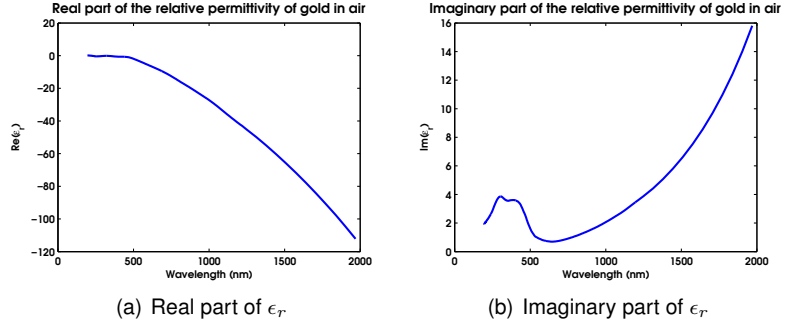


Figure 3.2: Relative permittivity of gold [20].

3.1.2 Laboratory and target frame

When dealing with DDSCAT you have to be careful about the directions and orientation of your target. DDSCAT uses two frames: the laboratory frame and the target frame. The lab frame is used to specify the propagation direction and polarization of the incident light wave. This frame is also used to specify the initial orientation of the target.

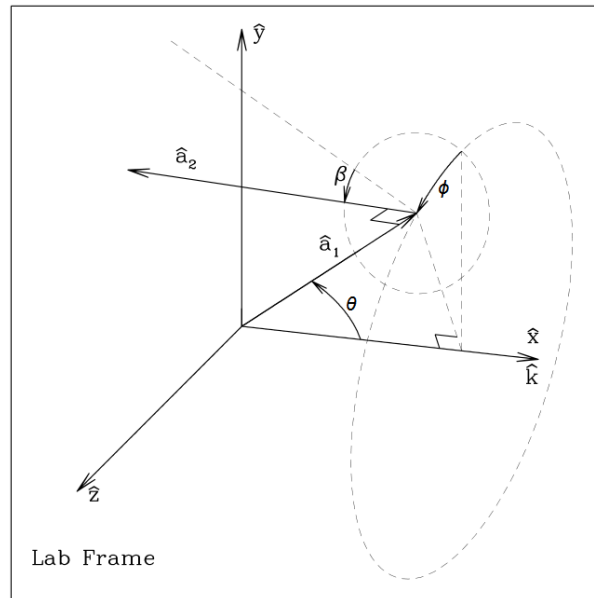


Figure 3.3: Orientation of the target frame relative to the laboratory frame [15].

The target can be turned through angles ϕ , θ and β as can be seen in figure 3.3. These angles specify the orientation of the target frame relative to the lab frame. The transformation from lab frame to target frame is as follows:

$$\hat{a}_1 = \hat{x}_{LF} \cos \theta + \hat{y}_{LF} \sin \theta \cos \phi + \hat{z}_{LF} \sin \theta \sin \phi \quad (3.1)$$

$$\hat{a}_2 = -\hat{x}_{LF} \sin \theta \cos \beta + \hat{y}_{LF} (\cos \theta \cos \beta \cos \phi - \sin \beta \sin \phi) + \hat{z}_{LF} (\cos \theta \cos \beta \sin \phi + \sin \beta \cos \phi) \quad (3.2)$$

$$\hat{a}_3 = \hat{x}_{LF} \sin \theta \sin \beta - \hat{y}_{LF} (\cos \theta \sin \beta \cos \phi + \cos \beta \sin \phi) - \hat{z}_{LF} (\cos \theta \sin \beta \sin \phi - \cos \beta \cos \phi) \quad (3.3)$$

Since all targets in this report are nanorods, and therefore symmetric around their long axis, rotation through β is pointless. When working with DDSCAT one always has to be careful about the frame of reference. DDSCAT generates output in both frames. For example, the electric field is computed in the target frame, whereas the torque is computed in the lab frame.

3.1.3 Accuracy

The parameter file has several options to increase the accuracy of the calculations. In the next few paragraphs the steps that were used in order to find the optimal balance between accuracy and calculation time are described.

Amount of dipoles

In order to determine the amount of dipoles that gives enough accuracy a few trial runs were done. Both effective radii of 20 nm and 60 nm were tested. For 20 nm an extinction spectrum was made around the dipole resonance frequency. The 60 nm particle was tested for wavelengths around its quadrupole resonance frequency. With each run the amount of dipoles was increased, until the spectra stopped changing significantly. This indicates the number of dipoles is sufficiently large. These simulations were done with a default error tolerance of 10^{-5} .

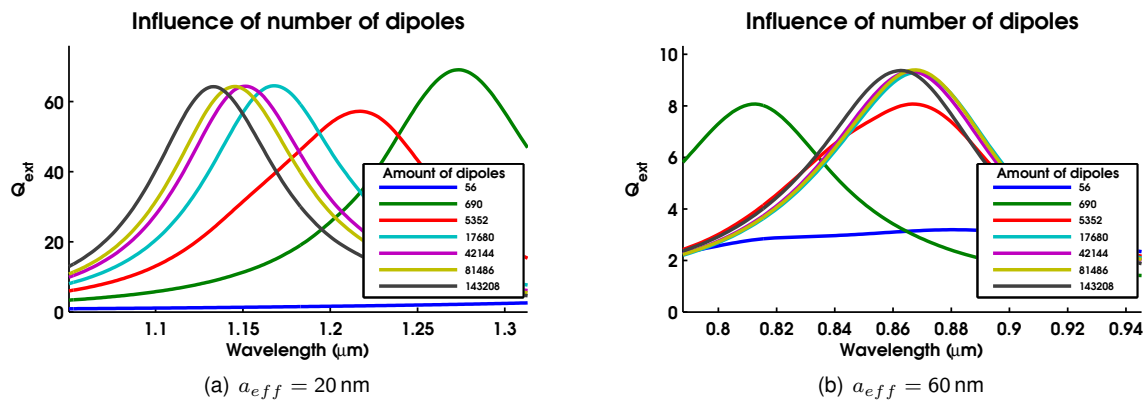


Figure 3.4: The influence of amount of dipoles on extinction spectra.

Based on the plots from figure 3.4 it was decided to run simulations with the amount of dipoles set between 15,000 and 20,000. Although the characteristics of the extinction spectra still shift slightly for even more dipoles, the shape of the curve is very similar. Moreover, a dipole amount larger than 20,000 will significantly increase computational time.

Error tolerance

In order to investigate the influence of the error tolerance on the results several extinction spectra were made with error tolerances of 10^{-1} , 10^{-2} , ..., 10^{-5} . This was done for wavelengths around the dipole resonance for a particle with $a_{eff} = 20 \text{ nm}$ and around the quadrupole resonance for $a_{eff} = 60 \text{ nm}$. Again, when the spectra do not show big differences any more, the error tolerance will be small enough. These simulations are done with 17680 dipoles.

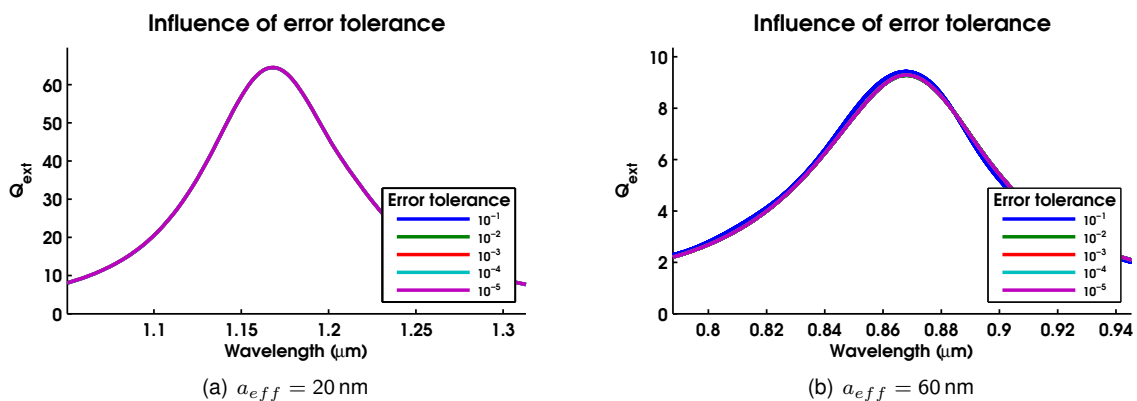


Figure 3.5: The influence of the error tolerance on extinction spectra.

The curves in figure 3.5 are almost identical for different values of the error tolerance. All simulations in this report are done with an error tolerance of 10^{-3} . Computation time for this value is not much longer than with a tolerance of 10^{-1} and ensures that enough iterations are done.

Particle size compared to wavelength

When looking at extinction spectra containing dipole and higher order multipole resonances, one has to bear in mind that the target should not be too big compared to the wavelength of the incident light. If the wavelength gets relatively small, the electric field varies over the length of the target particle and causes charge distributions that may look like the charge distribution of a higher multipole resonance (see figure 3.6). All simulations in this report were done with particles which length was at most one half times the wavelength of the incident light. DDSCAT always simulates the incident field with its maximum amplitude (E_0) at the center of the particle.

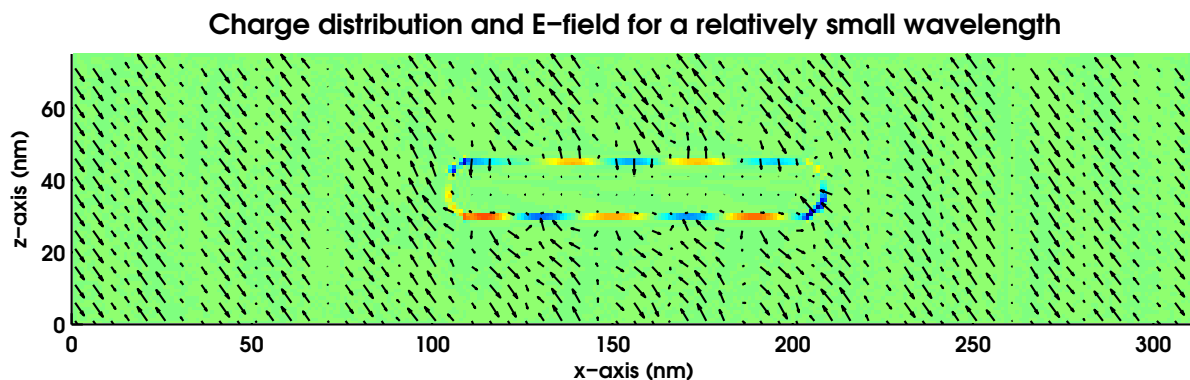


Figure 3.6: Charge distribution and E-field for small wavelength compared to particle size.

3.1.4 Near field calculations

DDSCAT is able to calculate the electric field that arises when a particle is hit by an incident light wave. This field can be used to study the surface charge distribution of the target. When the option NRFLD is selected in the parameter file, DDSCAT creates a binary file containing all information about the electric field. A program called `ddpostprocess` is included with the software. This program can read the binary files and output the intensity of the electric field or its components on a pre-specified line. In order to study the surface charge distribution, a section of Fortran code was added to the original `ddpostprocess`, which can be found in appendix E. The added section writes the components (real and imaginary) of the E-field and P-field as well as the composition of the target, polarizability tensor and dielectric function to separate text files. These files can be imported in Matlab for further analysis.

3.2 Processing with Matlab

Extinction and torque spectra

Matlab was used for all further processing in this report. For the extinction spectra and torque calculations, the needed values are read from the files created by DDSCAT and saved into an array. The dimensions of these arrays depend on which variables are varied during the simulation (wavelength, effective radius, θ and/or ϕ). These arrays can then be used to plot extinction or torque spectra.

Analysis of electric field

When analysing the electric field or charge distribution a different script is used. The output files created by `ddpostprocess` containing the E-field, P-field and the target composition are read into Matlab, as well as the total volume of computation. This is done by the code in Appendix F. All the fields are stored in 4D-arrays containing spatial data and vector components.

These arrays are then processed using the script in Appendix G. Since Matlab assumes that the rows represent the y-coordinate, a permutation is made to switch the x- and y-directions. To obtain

the charge distribution equation 2.11 is used. By looking at different cross sections of the particle, the electric field and charge distribution can be visualised. First the particle is drawn, using the composition data. Then the vector field is plotted, together with its corresponding field lines. These field lines are made using Matlab's streamline function on both the electric field and its negative counterpart in order to get a good overview. Finally the charge distribution is displayed in a separate image, together with an arrow representing the total dipole moment. This dipole moment can be calculated in two ways, as described in chapter 2.2. The dipole moment is computed in both ways, as a redundancy against errors.

Also, to validate the calculation the relation between P , α and E is checked. First the macroscopic field is converted to the microscopic field using equation 2.13 and then equation 2.14 is used to calculate the polarization at each point. Next the difference between the polarization that was just calculated and the polarization DDSCAT gives, is taken at each point. Finally, the mean of all these values is computed to get an average deviation. This number should be a couple percent of the average polarization at most.

Chapter 4

Results & Discussion

4.1 Extinction and torque spectra

The main purpose of this research is to investigate what happens to torque at the dipole, quadrupole and octupole resonances. In order to find out where the LSPR modes are and what happens at those wavelengths several extinction and torque spectra were made. By looking at different orientations and particle sizes, different order resonances can be analysed.

Aspect ratio

All simulations were executed for particles with an aspect ratio of 7. This aspect ratio was chosen because it provides a long axis that is long enough to see the quadrupole and octupole longitudinal modes. Furthermore, all modes redshift differently [1], making larger particles more suitable to be able to distinguish the different modes. An even bigger aspect ratio than 7 would increase computational time, while a smaller one would make the higher order resonances less visible. To illustrate this, an extinction spectrum was made for a particle with aspect ratio 3 (figure 4.1). The different modes are indicated by the dashed lines. It is easy to see that the transverse mode and the longitudinal quadrupole mode partly coincide, making this aspect ratio not suitable for our purposes.

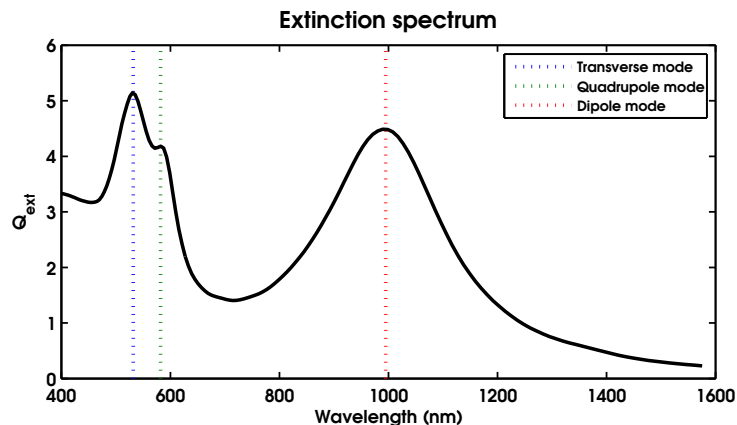


Figure 4.1: Extinction spectrum for a target with AR=3 and $r = 38$ nm, $\theta = 41^\circ$ and $\phi = 45^\circ$. Clearly, the transverse mode and quadrupole mode are badly distinguishable.

Angle dependence

In order to know for what orientations the simulations should be run, extinction plots were computed for several orientations. Both the extinction and torque were investigated and the results are displayed in figure 4.2. It is clearly visible that the largest torque occurs for $\theta = 41^\circ$. This is as expected since the torque is assumed to be maximal for an angle of 45° . This is due to the fact that the torque is proportional to $\sin(2\theta)$, as is derived in appendix C. Furthermore it can be noted that the quadrupole resonance is absent for $\theta = 0^\circ$ and $\theta = 90^\circ$, as is expected because of symmetry reasons [12–14]. The

final notable aspect of these plots is the fact that the shape of the torque spectrum of the quadrupole resonance changes significantly for different orientations, but this will not be further examined in this thesis.

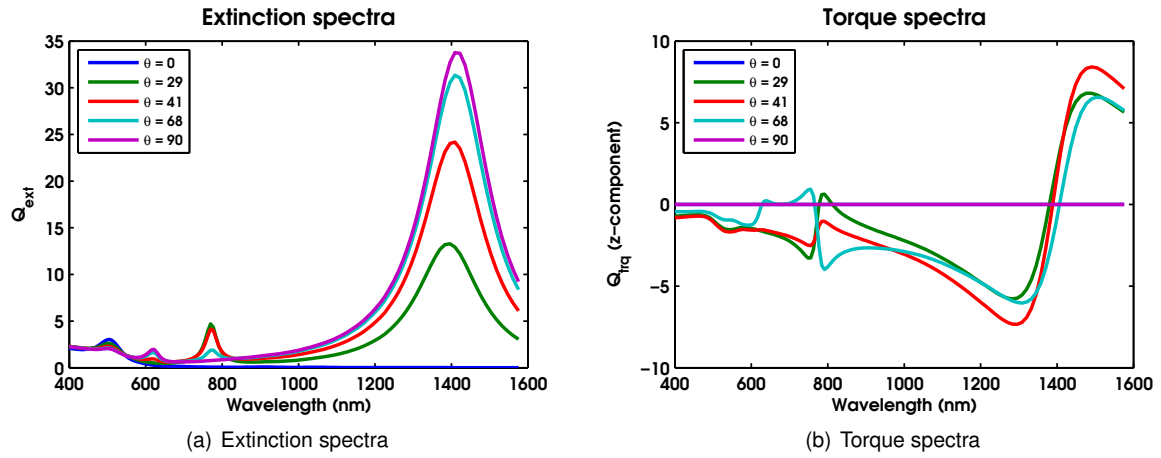


Figure 4.2: Extinction and torque spectra with different orientations, $r = 19 \text{ nm}$, $\phi = 45^\circ$.

For further investigation of the angle dependence of the extinction and torque efficiencies, plots are made of these quantities against θ , at a wavelength around the dipole resonance peak ($\lambda = 1500 \text{ nm}$). The expected relations are fitted to the data as well (figure 4.3). As expected, both fit a $\sin(2\theta)$ fairly well, although there is a slight shift towards larger angles. This can be explained by the fact that rotation through θ results in a phase difference of the incident field across the particle. Therefore for a certain angle the average incident field is slightly less than E_0 , thus the expected efficiency is obtained at a larger θ . When these plots are made for ϕ instead of θ this shift is not observed, because the incident field does not vary across the particle when rotating through ϕ .

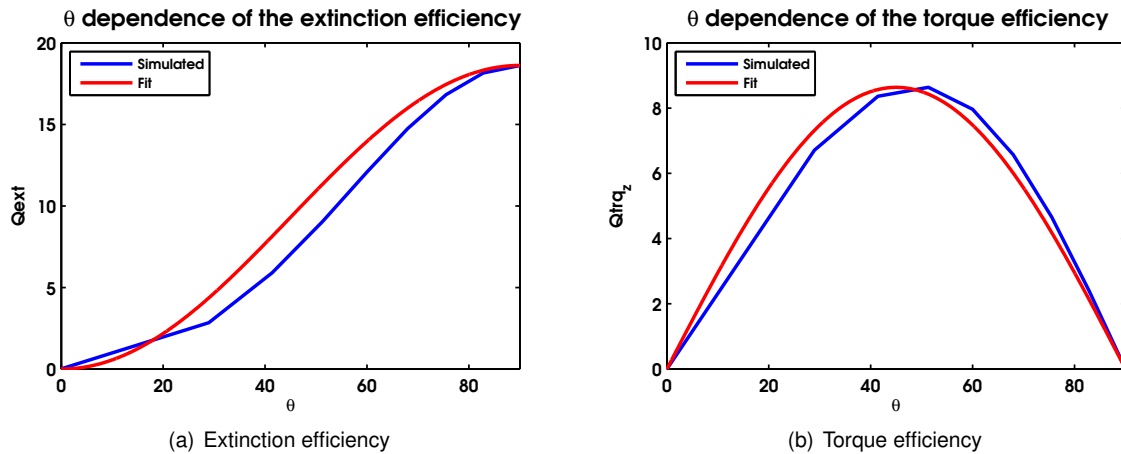


Figure 4.3: θ dependence of extinction and torque efficiency, $r = 19 \text{ nm}$, $\phi = 45^\circ$, $\lambda = 1500 \text{ nm}$.

Size dependence

The last parameter that is investigated is the influence of the size of the particle on the extinction and torque spectra. Spectra with a clear dipole resonance were simulated for different effective radii and the extreme values of these spectra are plotted to get information about the redshift that occurs. The size dependence of the extinction spectra is displayed in figure 4.4. The redshift is clearly visible for larger a_{eff} . For larger particles the redshift becomes bigger. These results confirm earlier findings by Kooij et al [1].

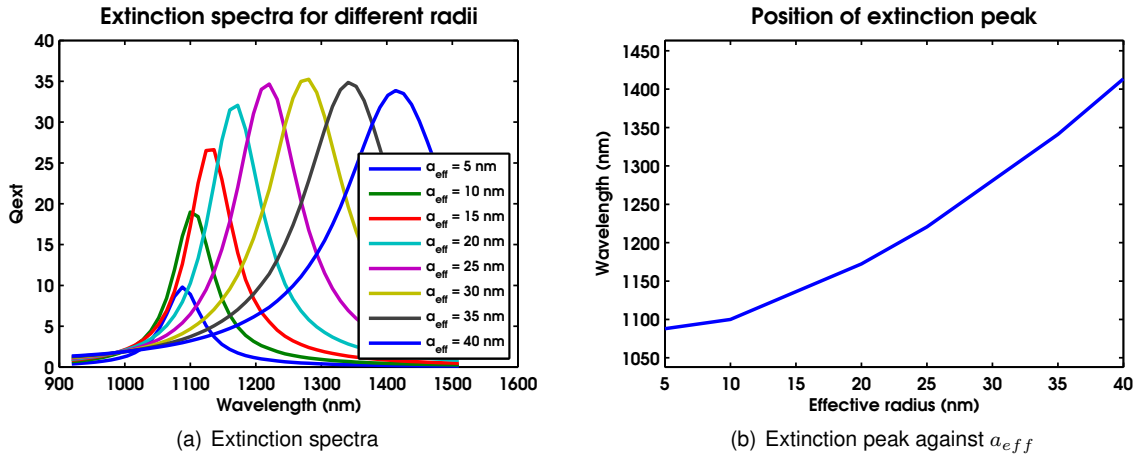


Figure 4.4: Size dependence of the extinction spectra, $AR=7$, $\theta = 90^\circ$, $\phi = 45^\circ$.

The torque spectra associated with the spectra from figure 4.4 can be seen in figure 4.5. The amount of redshift that occurs at each effective radius is very much alike the redshift for the extinction spectra.

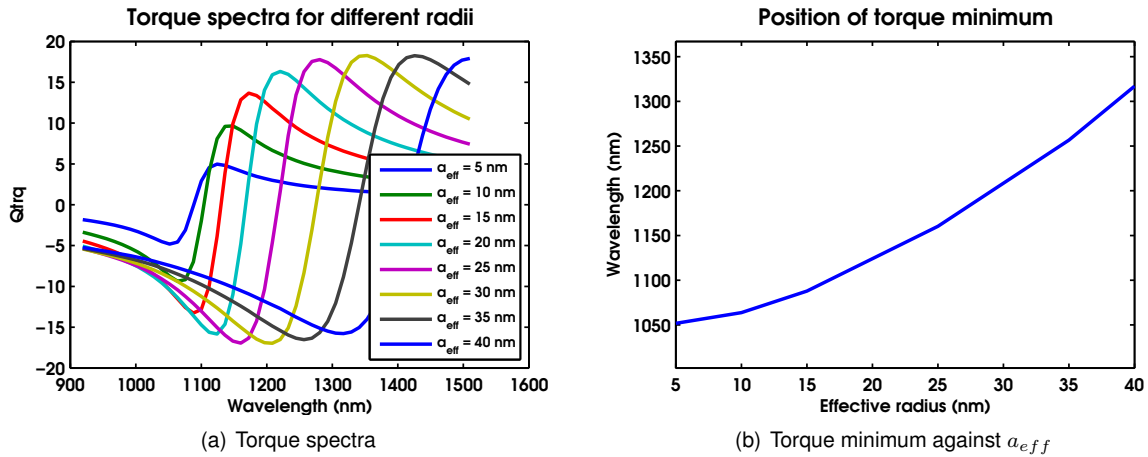


Figure 4.5: Size dependence of the torque spectra, $AR=7$, $\theta = 90^\circ$, $\phi = 45^\circ$.

4.1.1 Dipole

The dipole is the first order resonance of the LSPR. This was investigated for a target with an effective radius (referred to as a_{eff}) of 20 nm. This corresponds to a target short radius (referred to as r) of 9.3 nm. The relation between the effective radius and the target short radius can be found in Appendix A. In figure 4.6 both the extinction spectrum and the torque spectrum are displayed. One can clearly see a peak around $\lambda = 1170$ nm: the dipole resonance peak. The dotted lines indicate points around the peak that will be investigated further in section 4.2.1.

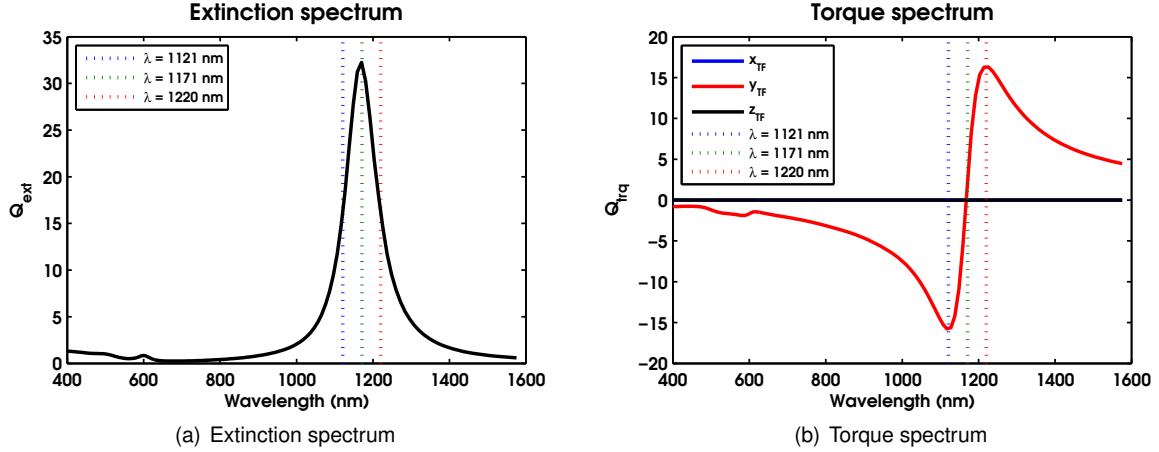


Figure 4.6: Extinction and torque spectra, $r = 9.3$ nm, $\phi = 45^\circ$, $\theta = 90^\circ$.

The torque changes sign in the dipole peak. This is a result of the change in sign of $Re(\alpha)$ as can be seen in figure 2.2. Since $\Gamma = \mathbf{p} \times \mathbf{E}$ and \mathbf{p} is proportional to α , it follows that the torque also changes sign. Based on figure 2.2 one would expect the peak to be located around 1000 nm. However, due to the redshifting caused by the size of the particle the peak has shifted approximately 150 nm.

4.1.2 Quadrupole

The quadrupole is the second order resonance of the LSPR. This peak is most pronounced for a larger particle ($a_{\text{eff}} = 60$ nm, $r = 28$ nm) oriented at $\phi = 0^\circ$ and $\theta \approx 30^\circ$. The particle has to be rotated through θ (i.e. in the $\mathbf{E}k$ -plane) to excite the quadrupole resonance, since even mode resonances are only visible for $0^\circ < \theta < 90^\circ$, due to earlier mentioned symmetry reasons. The quadrupole peak in the extinction spectrum is located around $\lambda = 860$ nm and the dashed lines again indicate points that will be investigated more later on. Since the target is significantly bigger than the one that was used for the dipole analysis, the dipole peak has redshifted to a bigger wavelength (≈ 1750 nm). Therefore, the dipole peak is only partly visible in figure 4.7.

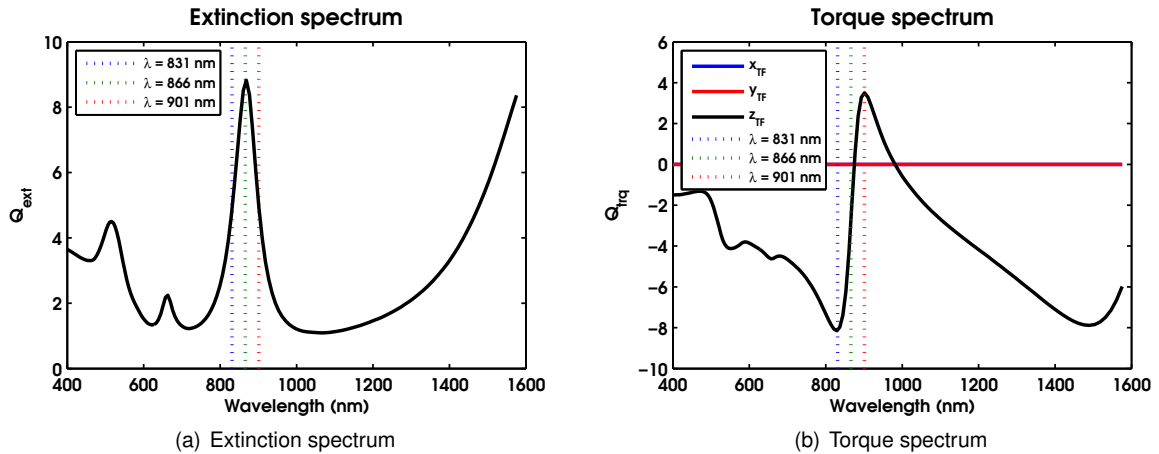


Figure 4.7: Extinction and torque spectra, $r = 28$ nm, $\phi = 0^\circ$, $\theta = 29^\circ$.

Around the quadrupole peak, the torque changes sign again. This would indicate that the quadrupole contribution causes $Re(\alpha)$ to change sign at this point. However, this explanation is not fully satisfactory, since a change of sign of $Re(\alpha)$ would only mean a flip in the charge distribution. But this would not have any effect on the dipole moment, as the quadrupole is an even, symmetric mode. Further note that the torque is not symmetric around zero, due to the still present contribution of the dipole peak.

4.1.3 Octupole

The octupole is the third order resonance of the LSPR. In order to observe an octupole, the target had to be relatively large again. Therefore the effective radius was set at 60 nm. Since the even resonance modes are only possible for a particle rotated through θ , θ was set at 90° . This way there is no influence of the quadrupole resonance. In the extinction spectrum, the octupole peak can be seen in the tail of the bigger dipole peak, which again is only partly visible. Note that the quadrupole peak vanishes entirely. Furthermore, the transverse mode is less pronounced in figure 4.8 than in figure 4.7. This is due to the more vertically oriented particle. The wavelengths indicated by the dashed lines will be investigated further in chapter 4.2.3.

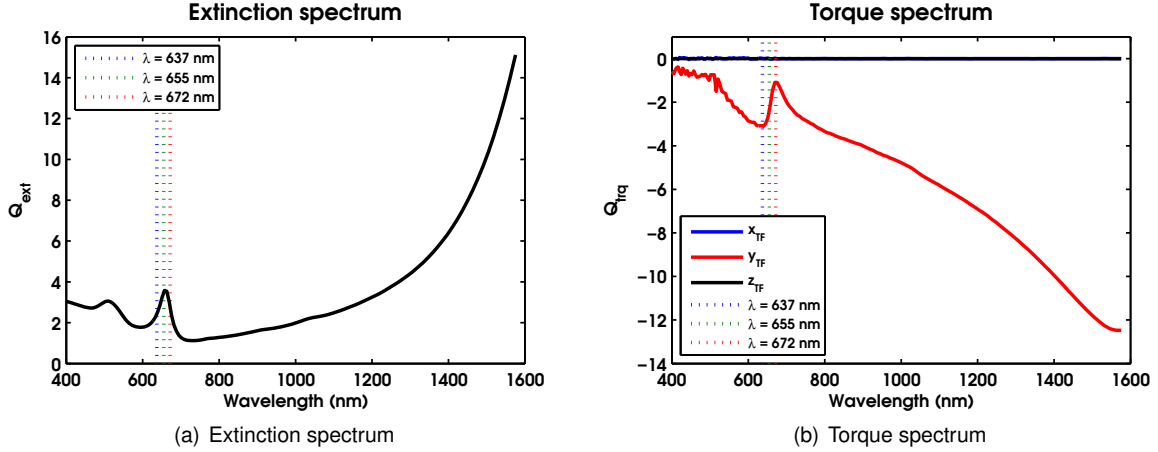


Figure 4.8: Extinction and torque spectra, $r = 28$ nm, $\phi = 45^\circ$, $\theta = 90^\circ$.

The octupole mode is visible in the torque spectrum as an oscillation. This time however, the torque does not change sign and therefore one would expect the net dipole moment to be oriented similar relative to the incident field for all wavelengths around this peak.

4.1.4 Possible torque

The torque is calculated using equation 2.3 solved for Γ and equation 2.4. u_{rad} is calculated by choosing a realistic value for the intensity I . This value is calculated using equation 2.5 with I set at 2×10^{11} W/m² [6]. Since the factor used for conversion between Q_{trq} and Γ is not wavelength dependent, the real torque spectrum would have completely the same shape as the spectrum for Q_{trq} . In order to find the most contributing mode the peak-to-peak amplitude of the different multipole contributions were calculated. These can be found in table 4.1. In order for all modes to be visible at the same time, θ was set at 41° and ϕ at 0° . However, this orientation does not render the optimal results for every individual mode.

	Dipole	Quadrupole	Octupole
$a_{eff} = 20$ nm	3.5×10^{-19} Nm	1.0×10^{-21} Nm	1.5×10^{-21} Nm
$a_{eff} = 40$ nm	1.7×10^{-18} Nm	8.3×10^{-20} Nm	—

Table 4.1: Peak-to-peak values of the torque for different a_{eff} and modes, $\phi = 0^\circ$, $\theta = 41^\circ$.

It can easily be seen that the dipole gives rise to the largest torque. Furthermore, the torque increases with the size of the particle, as one would expect. To find the maximum possible torque, the dipole mode should be investigated. In order to find the largest possible torque the target should only be rotated 45° through ϕ and not through θ , since the incident field will then be maximal across the entire target. a_{eff} was set at 40 nm. A larger effective radius would result in the dipole peak redshifting outside the available wavelength spectrum. The maximal torque amounts to $\Gamma = 1.15 \times 10^{-18}$ Nm. This is in agreement with values found experimentally [3, 6, 21].

In order to compare this torque with the energy of Brownian motion, equations 2.6–2.10 are used. These calculations approximate the nanorod as a cylinder submerged in water. This results in a rotational energy of 1.0×10^{-22} J. The energy involved with Brownian motion is in the order of kT or approximately 4.11×10^{-21} J. Therefore, this torque would not be enough to overcome Brownian rotation. However, this is not in agreement with the findings of Tong [6] and Ruijgrok [3], who found indications of possible alignment for similar torque values. Furthermore, de Abajo [21] also claims (without further explanation) that a torque of this order is large enough to overcome Brownian motion. Ruijgrok uses a different method to compare the torque to Brownian motion. He calculates the potential energy via a Boltzmann distribution and compares this to kT . When this method is applied to our findings, this results in an energy of 9.2×10^{-15} J. This would be orders of magnitude larger than kT and Brownian motion should easily be overcome. This might indicate that the energy analysis that was applied in this report is not entirely valid. Note that despite the ambiguity between the energies, the torque values are highly comparable.

4.2 Charge distribution

In this section the different resonances will be investigated further. This is done by doing near field calculations for wavelengths near the resonance peaks. The electric fields are illustrated in two types of figures. The first being an image of the electric field lines. These lines hold no information about the direction of the field or the intensity, but they illustrate the general outline of the electric field, i.e. it becomes clear whether the field is that of a dipole, quadrupole or octupole. The second image displays the macroscopic charge distribution. For all images the colors represent the charge density. Red indicates positive charge and blue means negative charge. These images also have the net dipole moment of the target depicted as a red arrow. These arrows are not equally scaled, the dipole moments for the dipole resonance are scaled ten times smaller than those for the quadrupole and octupole resonances.

4.2.1 Dipole

From the extinction and torque spectra around the dipole peak it is clear that a flip occurs. Since the torque changes sign in this regime, it seems logical to expect some change in the surface charge distribution, and therefore the resulting electrical field, of the target particle. This can be investigated by looking at the charge distribution and E-field for different wavelengths around the dipole peak. These results are displayed in figures 4.9, 4.10, 4.11. The polarization accuracy check gives an average deviation of 0.17%, which indicates a valid solution.

The particle exhibits dipole behaviour at points around the dipole peak. However, the field is slightly skewed in the direction of the incident field. It is clear that with progressing wavelengths, the entire dipole turns around. As a result, the torque switches sign as well. Moreover, at the top of the dipole peak, the dipole moment is quite small. Because of that the incident E-field gets hardly disturbed by the scattered field from the particle, which results in almost parallel field lines as would be the case if there were only the incident field. This also results in a charge distribution on the particle that is induced by the incident field. The top of the target is slightly negatively charged and the bottom is slightly positive, which causes an electric field in the particle opposite to the incident field.

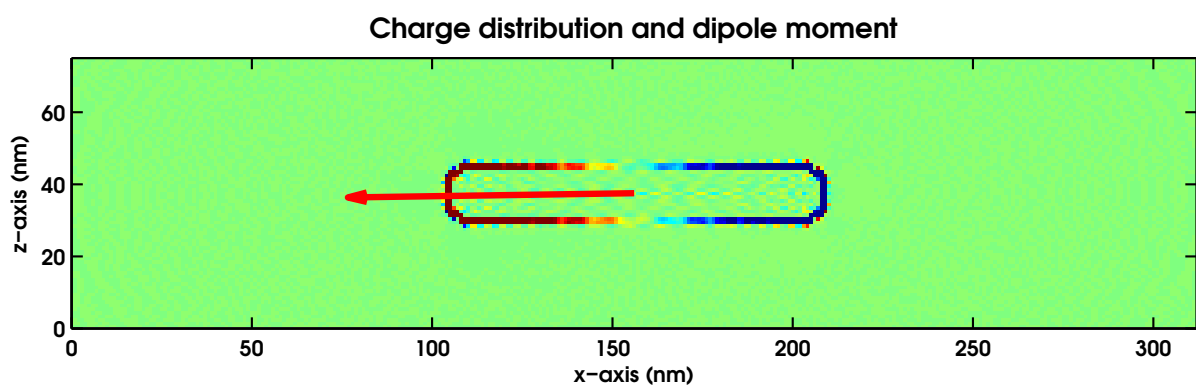
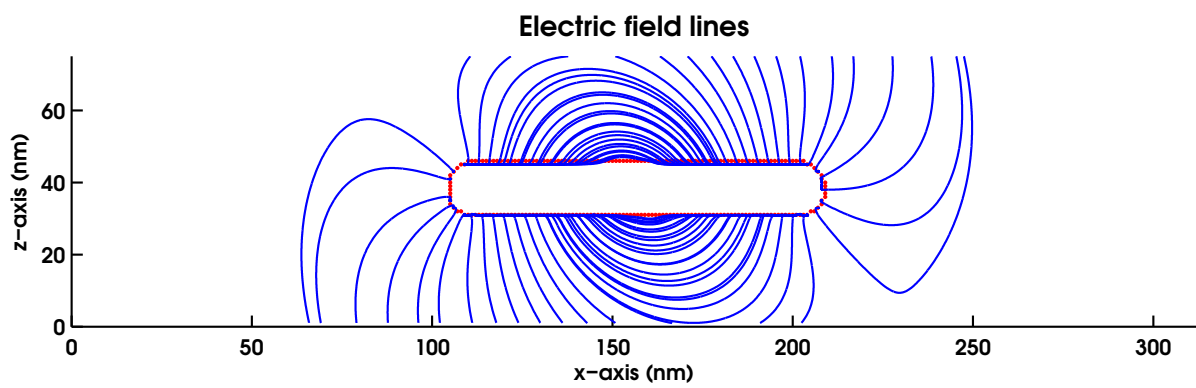


Figure 4.9: Electric field just left of the dipole peak at $\lambda = 1121$ nm, $r = 9.3$ nm, $\phi = 45^\circ$, $\theta = 90^\circ$.

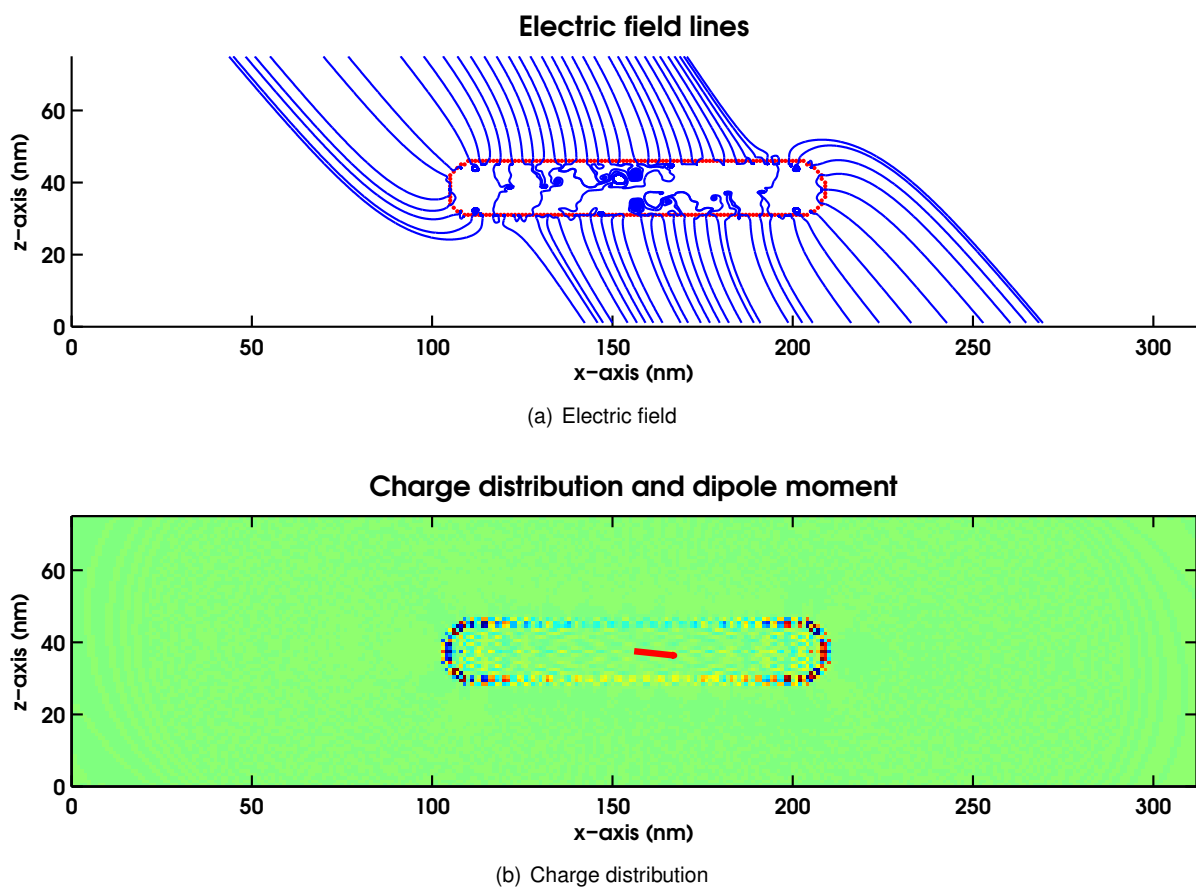


Figure 4.10: Electric field at the top of the dipole peak at $\lambda = 1171$ nm, $r = 9.3$ nm, $\phi = 45^\circ$, $\theta = 90^\circ$.

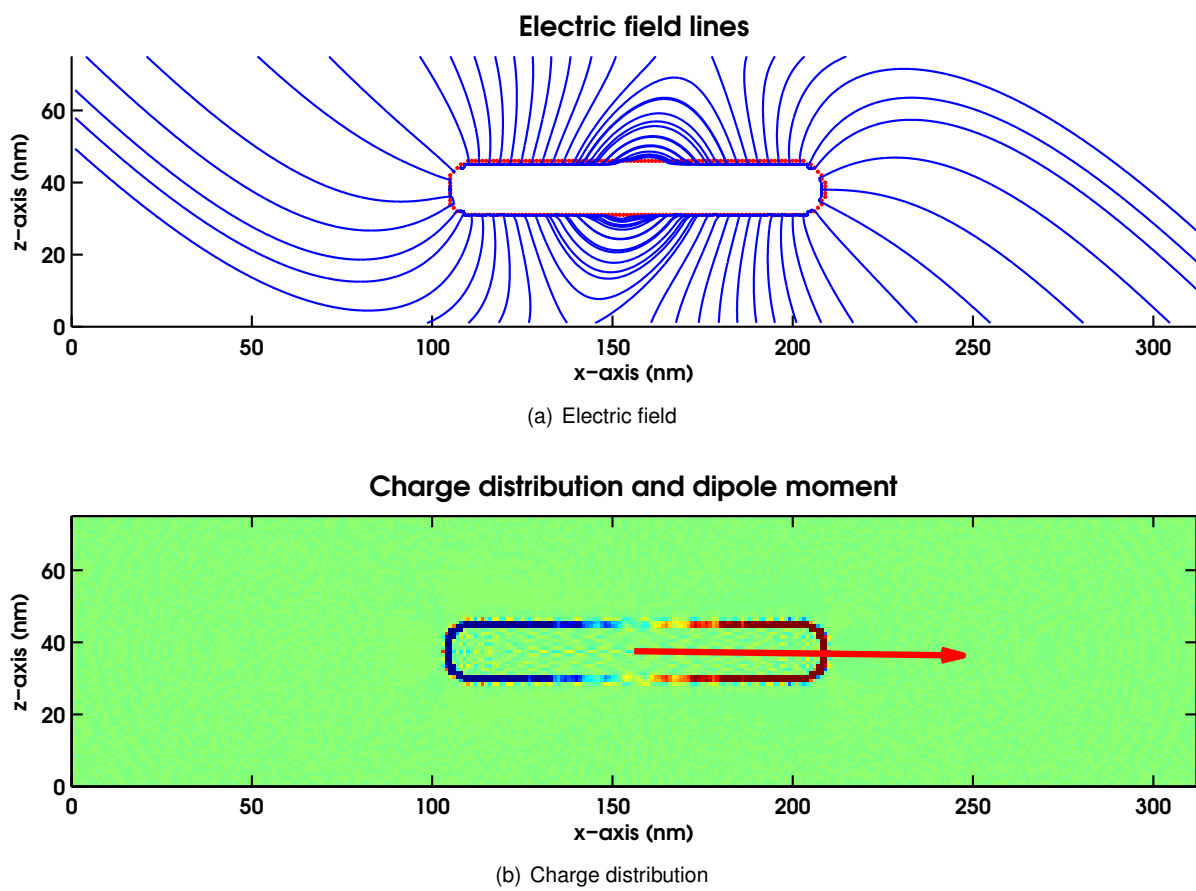


Figure 4.11: Electric field just right of the dipole peak at $\lambda = 1220$ nm, $r = 9.3$ nm, $\phi = 45^\circ$, $\theta = 90^\circ$.

4.2.2 Quadrupole

Next the quadrupole resonance is investigated. These results can be seen in figure 4.12, 4.13, 4.14. The polarization accuracy check gives an average deviation of 0.2%. From these figures it becomes clear that the electric field does not change very much for different wavelengths around the quadrupole resonance. The same holds for the charge distribution. Although the intensity varies, the symmetry remains the same. Note that the quadrupole is most intense at its resonance peak, contrary to the dipole peak. This would indicate that the quadrupole contribution to the polarizability is at a maximum in the quadrupole peak. The quadrupole clearly is asymmetrical. This is due to the incident field, which amplifies the positive pole on one side of the target and weakens the pole on the other side.

From the torque spectrum in figure 4.7b one would expect the torque to change sign. Therefore it seems logical to expect some shift of charge. However, this is not the case as can also be seen by looking at the net dipole moments. They hardly change in both size and direction. The fact that there is a torque can be explained by the asymmetry in the charge distribution. Normally a quadrupole or any other pure multipole would not have a net dipole moment and therefore would not give rise to a torque. In this case however, the charge distribution gets shifted because of the external field. This results in a net dipole moment and thus in a net torque, although it does not explain why the torque changes sign in the torque spectrum without any apparent change in charge distribution.

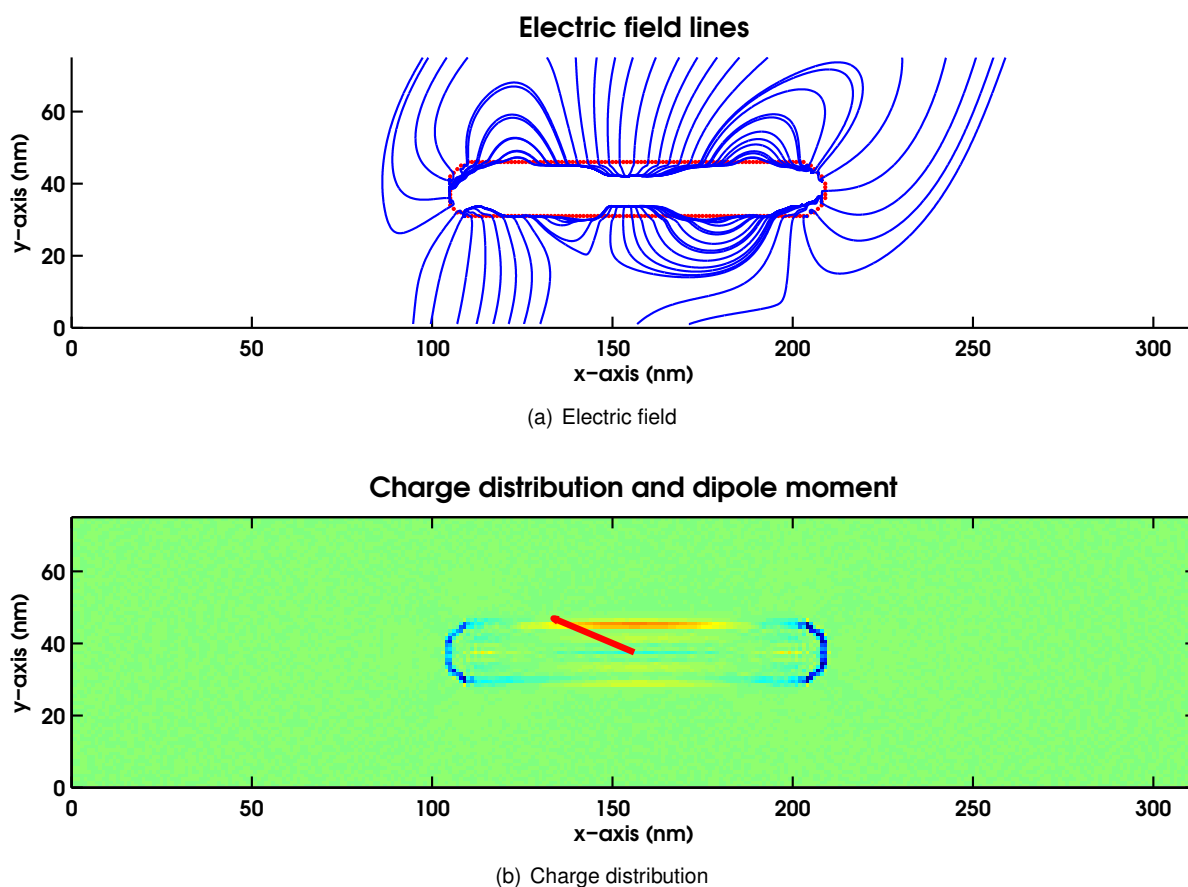


Figure 4.12: Electric field just left of the quadrupole peak at $\lambda = 831$ nm, $r = 28$ nm, $\phi = 0^\circ$, $\theta = 29^\circ$.

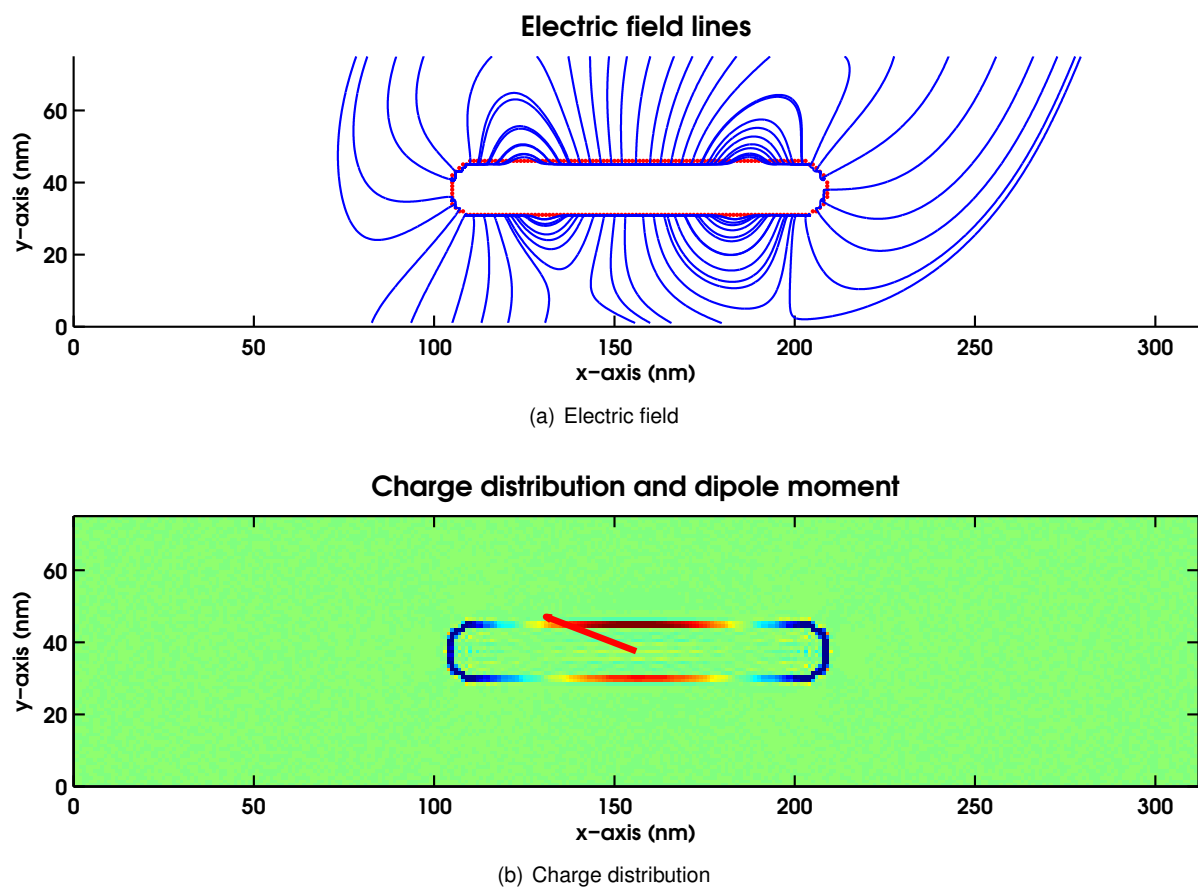


Figure 4.13: Electric field at the top of the quadrupole peak at $\lambda = 866 \text{ nm}$, $r = 28 \text{ nm}$, $\phi = 0^\circ$, $\theta = 29^\circ$.

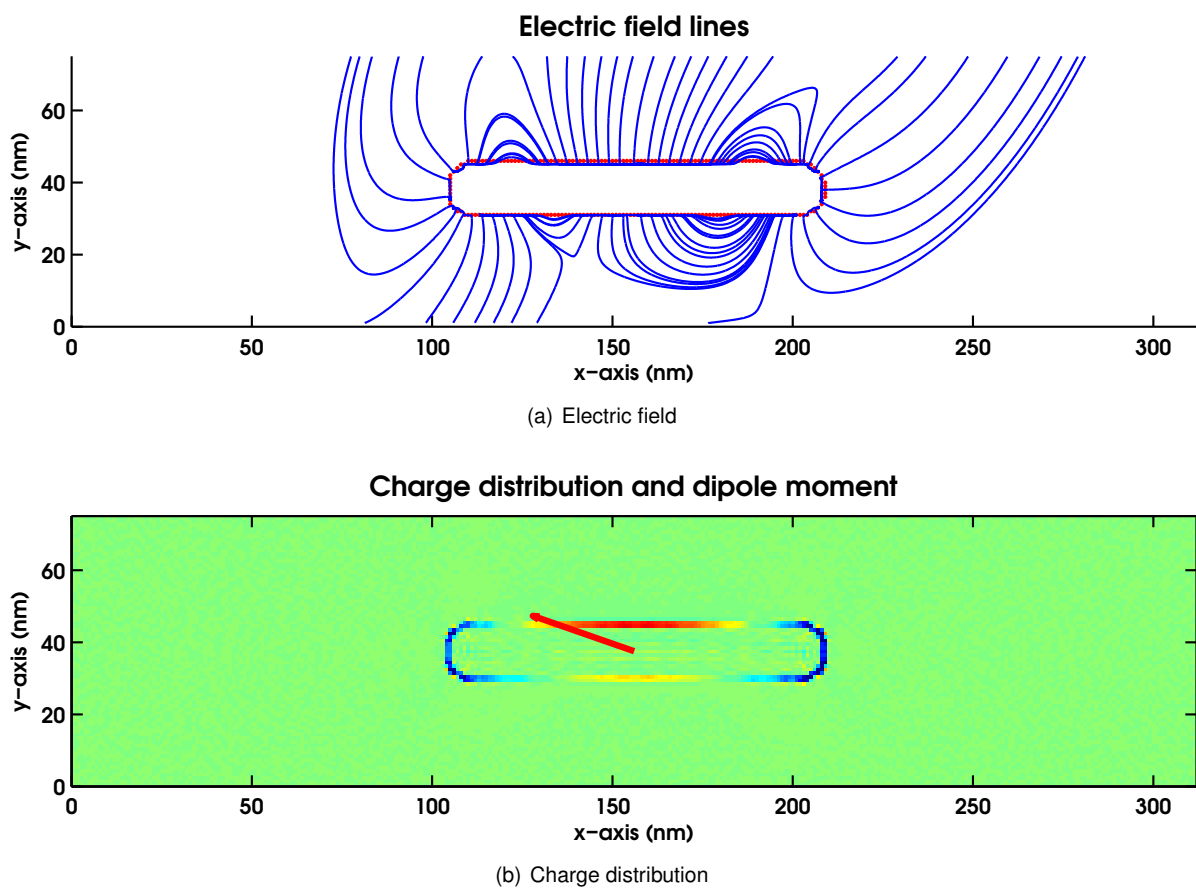


Figure 4.14: Electric field just right of the quadrupole peak at $\lambda = 901$ nm, $r = 28$ nm, $\phi = 0^\circ$, $\theta = 29^\circ$.

4.2.3 Octupole

The last resonance mode that is looked into further is the octupole mode, of which the results are displayed in figure 4.15, 4.16, 4.17. The polarization accuracy check gives an average deviation of 0.17%. Clearly an octupole resonance can be seen, characterised by the six alternating charge patches on the surface of the target. It must be noted that this mode is similar to the dipole in the way that they are both asymmetrical modes. Both have opposite charge at the ends of the target, therefore inducing a net dipole moment. Another similarity between the dipole and octupole is that the real part of the octupole contribution to the polarizability seems to be 0 at the peak of the resonance.

At the wavelengths that are displayed an inversion of the charge distribution can be seen, alike the dipole. At first this would suggest a change of sign of the torque. However, when looking closely at the net dipole moment, one can see that it rotates, but it stays on the left hand side of the incident field. This is consistent with the results from the torque spectrum in figure 4.8b. The torque does change for the different wavelengths, but its sign remains the same due to an offset created by the dipole. Since the torque is a result of a cross product of the dipole moment and the electric field it will be maximum when these are perpendicular, resulting in a relatively large torque, either positive or negative depending on orientation. At $\lambda = 637$ nm the net dipole moment is almost perpendicular to the incident field. This corresponds to the local minimum in figure 4.8b. At $\lambda = 672$ nm the dipole moment has rotated towards the electric field, resulting in a smaller torque, just as one would expect from the torque spectrum.

At the peak of the octupole resonance, almost all octupole behaviour is gone. What is left is a charge distribution that opposes the incident field as was the case for the dipole. The x-component of the net dipole moment is a result of the octupole being located in the tail of the dipole peak.

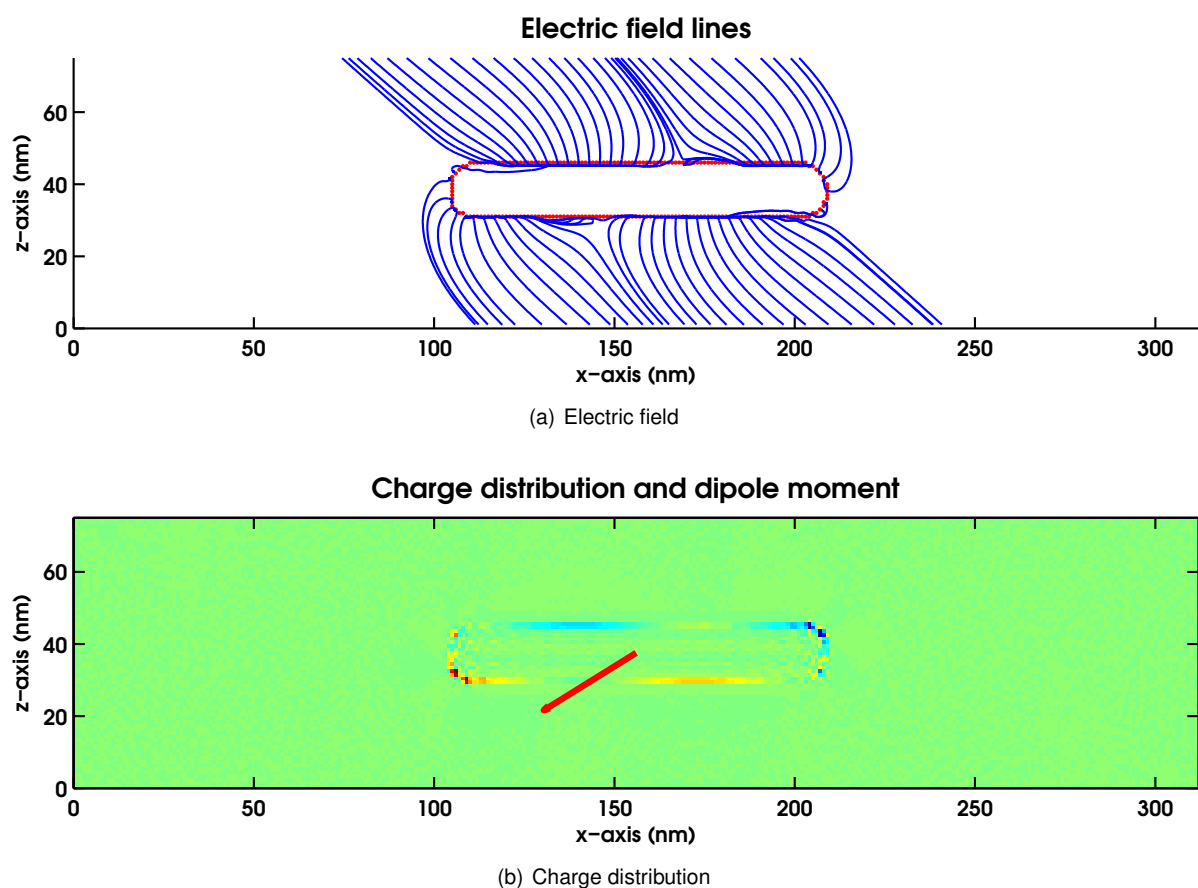


Figure 4.15: Electric field just left of the octupole peak at $\lambda = 637$ nm, $r = 28$ nm, $\phi = 45^\circ$, $\theta = 90^\circ$.

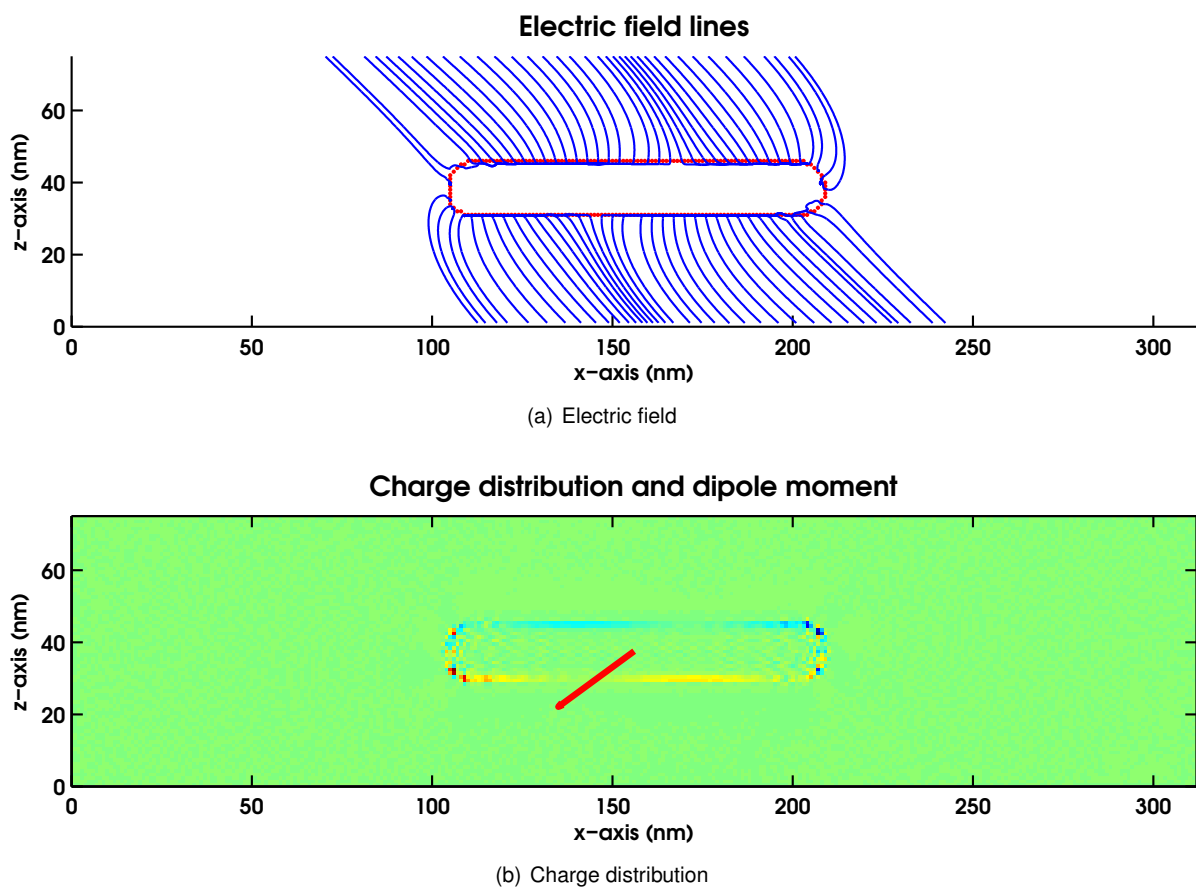


Figure 4.16: Electric field at the top of the octupole peak at $\lambda = 655$ nm, $r = 28$ nm, $\phi = 45^\circ$, $\theta = 90^\circ$.

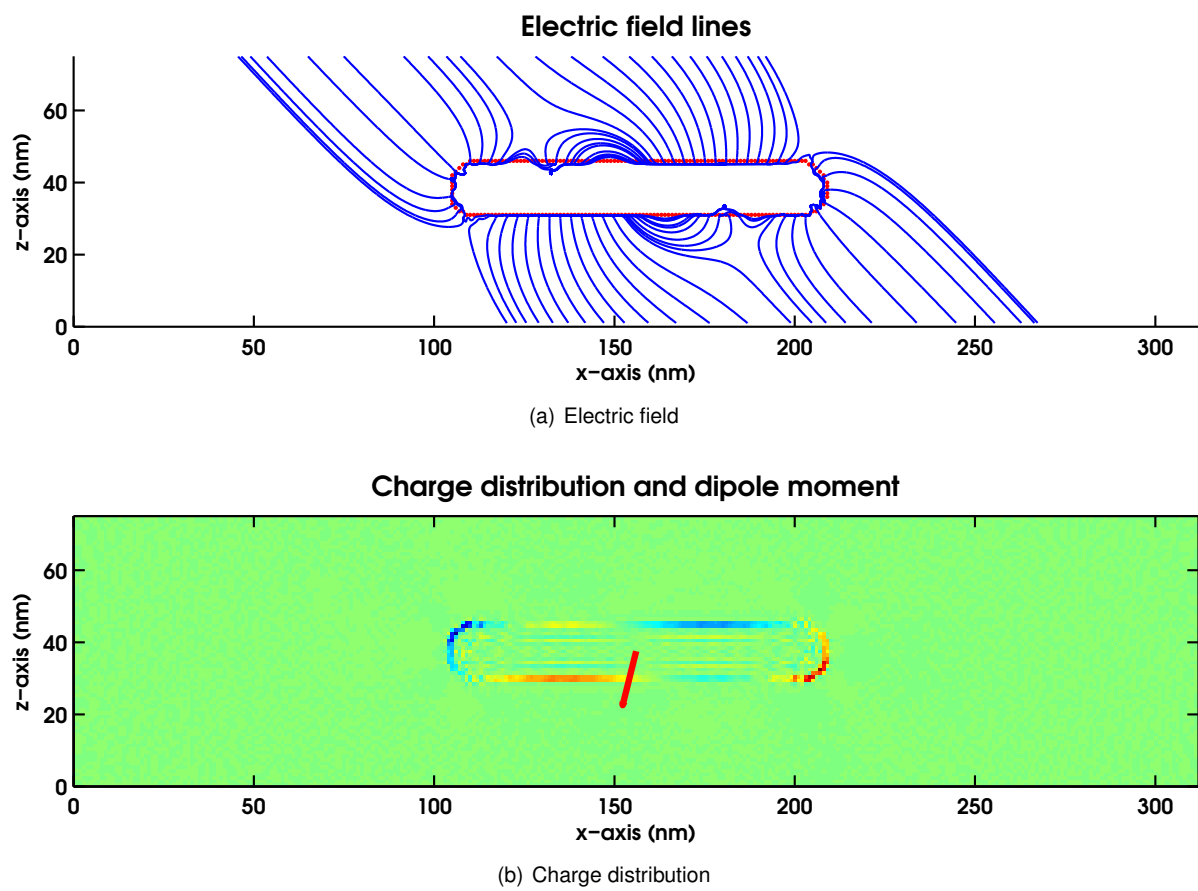


Figure 4.17: Electric field just right of the octupole peak at $\lambda = 672$ nm, $r = 28$ nm, $\phi = 45^\circ$, $\theta = 90^\circ$.

4.3 Improvements and recommendations

For future research, a few improvements can be made. First of all, one could use more dipoles for more accurate results. In order to do so, one needs more computational power, since this will take a significant amount of time. In this report the angle dependence of the torque is not looked into, although there were some notable features visible in the spectra for the quadrupole modes. This might be of interest for explaining the unclear quadrupole torque oscillation. By doing some nearfield calculations for different orientations one may get more insight in this phenomenon.

Another possibility is looking at different aspect ratios. Even bigger aspect ratios will likely cause higher order resonances to appear in the spectra. This way one could research other even modes (hexadecupole etc.) in order to see if they behave alike the quadrupole. This again will require more computational power and/or time.

Finally, one could look into larger particle dimensions. Similar to bigger aspect ratios this will give rise to higher order resonances. Furthermore, one could investigate the torque for these larger particles to find if it is large enough to overcome Brownian motion.

Chapter 5

Conclusion

The properties of gold nanorods have been investigated with a special focus on the optical torque induced by surface plasmon resonances. In order to do this, extinction spectra have been simulated together with a visualisation of the charge distribution on the target surface. All particles showed clearly visible resonance peaks in their extinction spectra as well as an associated oscillation in their torque spectrum. Not only the odd dipole and octupole modes, but also the even quadrupole mode exhibit this behaviour. The oscillation in the torque spectra suggest a shifting symmetry of the charge distribution. For the dipole and octupole this seems logical since they have opposite charges at both ends of the target. Since $Re(\alpha)$ changes sign at the resonance peak, the torque oscillation can be explained by the fact that the charge distribution gets inverted. However, for the quadrupole the charge distribution has the same symmetry axes as the target and therefore a flip of the charge distribution would not change the situation. Moreover, there is no flip in charge visible for the quadrupole resonance.

When analysing the electric field and the charge distribution it was found that the dipole resonance resulted in the largest dipole moment, which confirms that this also gives rise to the largest torque values. The shift in the charge distribution was observed for the dipole and octupole modes, thus confirming the presumption on the origin of the torque oscillation. For the quadrupole mode, no shift was observed in the charge distribution. Instead of getting weaker at the resonance peak, the quadrupole was at its strongest at that wavelength. This suggests that $Re(\alpha)$ does not change sign there, but instead is at a maximum. It is unclear how the quadrupole, with these charge distributions and associated dipole moments, can result in a torque oscillation. Since the dipole moments remain nearly identical and the electric field also remains very similar one would not expect a sudden change in the optical torque, yet this change is visible in the torque spectrum.

The maximum torque was achieved for the dipole resonance at an angle of approximately 45° relative to the polarization of the incident light. For an effective radius of 40 nm and an intensity of $2 \times 10^{11} \text{ W/m}^2$ this torque amounted to $1.15 \times 10^{-18} \text{ Nm}$. This is in accordance with experimentally determined values [3, 6, 21]. The rotational energy that corresponds with this torque is $1.0 \times 10^{-22} \text{ J}$ and would not be sufficient for optical alignment. However, when using a different energy analysis, this torque would suffice as indicated by the experimental results. This might indicate an invalidity in the energy analysis that was used in this thesis.

Chapter 6

Acknowledgements

As Geoffrey Chaucer said: *'All good things must come to an end'*, and so must this thesis. Therefore we would like to thank some people that helped us carry out our bachelor assignment. In the first place we would like to thank Stefan Kooij as our personal supervisor, who helped us with the problems we encountered and provided us with tons of information on our subject. We would also like to thank the rest of our graduation committee for taking the time to read and comment on our work. In addition we thank the whole group of PIN for making us feel welcome and for the good company during the coffee breaks.

A special thanks we owe to Bruce Draine, developer of the DDA software. He helped us overcome some difficulties we had with the software and immediately sent us an updated package of DDSCAT to help us when we encountered a few bugs. Despite the fact that he undoubtedly is a very busy man he responded to all our messages quickly, even during his holidays.

Finally we would like to thank everyone who supported us during this summer.

Bibliography

- [1] E.S. Kooij, W. Ahmed, H.J.W. Zandvliet, and B. Poelsema. Localized plasmons in noble metal nanospheroids. *The Journal of Physical Chemistry C*, 115(21):10321–10332, 2011.
- [2] D.J. Griffiths. *Introduction to electrodynamics*. Prentice Hall, Upper Saddle River, N.J, 1999.
- [3] P.V. Ruijgrok, N.R. Verhart, P. Zijlstra, A.L. Tchebotareva, and M. Orrit. Brownian fluctuations and heating of an optically aligned gold nanorod. *Phys. Rev. Lett.*, 107:037401, Jul 2011.
- [4] C. Rockstuhl and J. Tominaga. Calculation of the torque exerted by light fields on silver elliptical nanocylinders. *EPL (Europhysics Letters)*, 73(2):313, 2006.
- [5] J.W. Liaw, W.J. Lo, and M.K. Kuo. Wavelength-dependent longitudinal polarizability of gold nanorod on optical torques. *Opt. Express*, 22(9):10858–10867, May 2014.
- [6] L. Tong, V.D. Miljkovic, and M. Kall. Alignment, rotation, and spinning of single plasmonic nanoparticles and nanowires using polarization dependent optical forces. *Nano Letters*, 10(1):268–273, 2010. PMID: 20030391.
- [7] C.F. Bohren and D.R. Huffman. *Absorption and scattering of light by small particles*. Wiley, New York, 1983.
- [8] E.S. Kooij and B. Poelsema. Shape and size effects in the optical properties of metallic nanorods. *Phys. Chem. Chem. Phys.*, 8:3349–3357, 2006.
- [9] B.T. Draine and J.C. Weingartner. Radiative torques on interstellar grains. i. superthermal spinup. *The Astrophysical Journal*, 470, 1996.
- [10] U. Kreibig. *Optical properties of metal clusters*. Springer, Berlin New York, 1995.
- [11] W.T. Doyle and I.S. Jacobs. The influence of particle shape on dielectric enhancement in metal-insulator composites. *Journal of Applied Physics*, 71(8):3926–3936, 1992.
- [12] B.N. Khlebtsov and N.G. Khlebtsov. Multipole plasmons in metal nanorods: scaling properties and dependence on particle size, shape, orientation, and dielectric environment. *The Journal of Physical Chemistry C*, 111(31):11516–11527, 2007.
- [13] E.R. Encina and E.A. Coronado. Resonance conditions for multipole plasmon excitations in noble metal nanorods. *The Journal of Physical Chemistry C*, 111(45):16796–16801, 2007.
- [14] E.K. Payne, K.L. Shuford, S. Park, G.C. Schatz, and C.A. Mirkin. Multipole plasmon resonances in gold nanorods. *The Journal of Physical Chemistry B*, 110(5):2150–2154, 2006.
- [15] B.T. Draine and P.J. Flatau. *User Guide for the Discrete Dipole Approximation Code DDSCAT 7.3*, May 2013.
- [16] K. Bonin, B. Kourmanov, and T. Walker. Light torque nanocontrol, nanomotors and nanorockers. *Opt. Express*, 10(19):984–989, Sep 2002.
- [17] B.T. Draine and P.J. Flatau. Discrete-dipole approximation for scattering calculations. *J. Opt. Soc. Am. A*, 11(4):1491–1499, Apr 1994.
- [18] P.J. Flatau and B.T. Draine. Fast near field calculations in the discrete dipole approximation for regular rectilinear grids. *Opt. Express*, 20(2):1247–1252, Jan 2012.

-
- [19] T.K. Sau and C.J. Murphy. Seeded high yield synthesis of short au nanorods in aqueous solution. *Langmuir*, 20(15):6414–6420, 2004.
- [20] E. Palik. *Handbook of optical constants of solids III*. Academic Press, San Diego, 1998.
- [21] F.J.G. de Abajo. Electromagnetic forces and torques in nanoparticles irradiated by plane waves. *Journal of Quantitative Spectroscopy and Radiative Transfer*, 89(14):3 – 9, 2004. {VII} Electromagnetic and Light Scattering by Non-Spherical Particles: Theory, Measurement, and Applications.
- [22] K.A. Willets and R.P. Van Duyne. Localized surface plasmon resonance spectroscopy and sensing. *Annual Review of Physical Chemistry*, 58(1):267–297, 2007. PMID: 17067281.
- [23] C. Kittel. *Introduction to solid state physics*. Wiley, Hoboken, NJ, 2005.

Appendix A

Effective radius

For all different target geometries DDSCAT uses the same measure for the size of the particle: the effective radius. The effective radius is the radius of a sphere of the same volume as the target. Since the target geometry used throughout this thesis is the capped cylinder, a conversion has to be made between the effective and short radius of the target. DDSCAT uses the two shape parameters to determine the shape of the target.

$$\text{SHPAR}_1 = \frac{\text{cylinder length}}{d} \quad (\text{A.1})$$

$$\text{SHPAR}_2 = \frac{\text{cylinder diameter}}{d} \quad (\text{A.2})$$

where d is the dipole spacing and SHPAR are the shape parameters. This results in the total length of the target being: $(\text{SHPAR}_1 + \text{SHPAR}_2)d$. In order to find the short radius of the target as a function of the effective radius, the following equation must be solved:

$$\frac{4}{3}\pi a_{eff}^3 = 2\pi r^3(AR - 1) + \frac{4}{3}\pi r^3 \quad (\text{A.3})$$

With a_{eff} the effective radius, r the short radius of the target and AR the aspect ratio that is used. That gives for the short radius:

$$r = \frac{2a_{eff}}{\sqrt[3]{4(3AR - 1)}} \quad (\text{A.4})$$

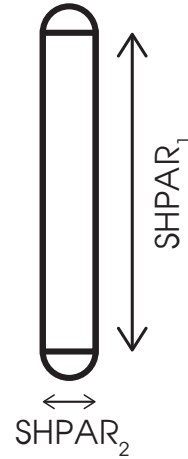


Figure A.1: Schematic drawing of a target particle.

Appendix B

Macroscopic vs. microscopic field

DDSCAT only gives the macroscopic field as an output. However, it is possible to convert between the macroscopic and microscopic electric fields. Among other equations, the Clausius-Mossotti relation is needed for this conversion. The following derivation starts with the Clausius-Mossotti relation and is done in Gaussian units:

$$\frac{\epsilon - 1}{\epsilon + 2} = \frac{4\pi\alpha n}{3} \quad (\text{B.1})$$

Together with:

$$\mathbf{D} = \epsilon \mathbf{E}_{macro} = \mathbf{E}_{macro} + 4\pi \mathbf{P} \quad (\text{B.2})$$

And:

$$\mathbf{P} = n\alpha \mathbf{E}_{micro} \quad (\text{B.3})$$

Then follows:

$$\mathbf{E}_{micro} = \left(\frac{\epsilon + 2}{3} \right) \mathbf{E}_{macro} \quad (\text{B.4})$$

Where ϵ is the permittivity, α the polarizability, n the atomic density of the molecules, \mathbf{D} the electric displacement field and \mathbf{P} the polarization [15, 23].

Ambiguity regarding the microscopic field

In this report the macroscopic field has been used for all calculations concerning the electric field. This is valid since extinction and torque are treated as far field phenomena. Therefore, the field inside the particle is irrelevant. However, during the calculations of the dipole moments, a peculiar observation was done. While the macroscopic electric field and the polarization field resulted in two dipole moments in almost perfect agreement with each other, the microscopic field resulted in a dipole moment exactly $2/3$ of the dipole moment following from the macroscopic field.

One could assume that these net dipole moments should not show any discrepancy, since the macroscopic field is an averaged version of the microscopic field. Therefore, a summation over all microscopic dipoles should render the same results as a macroscopic calculation. Up to now it is unclear where this factor of $2/3$ comes from. There might be an error in the relation between the microscopic and macroscopic fields, or maybe, since the software hardly uses the microscopic field, it might not be suitable for this type of calculations. This ambiguity does not affect our results, because only the macroscopic field is used and both ways of calculating the dipole moment give matching results.

Appendix C

Angle dependence of torque

It is possible to derive the angle dependence of the torque. Start by solving the cross product in equation 2.2, which gives:

$$\begin{aligned}\tau &= \mathbf{p} \times \mathbf{E} \\ &= \alpha E_{\parallel} E_{\perp} \\ &= \alpha E \sin(\theta) E \sin(90 - \theta) \\ &= \alpha E^2 \sin(\theta) \cos(\theta) \\ &= \frac{1}{2} \alpha E^2 \sin(2\theta)\end{aligned}\tag{C.1}$$

From this we can conclude that the torque is proportional to $\sin(2\theta)$ and should therefore be maximal at $\theta = 45^\circ$.

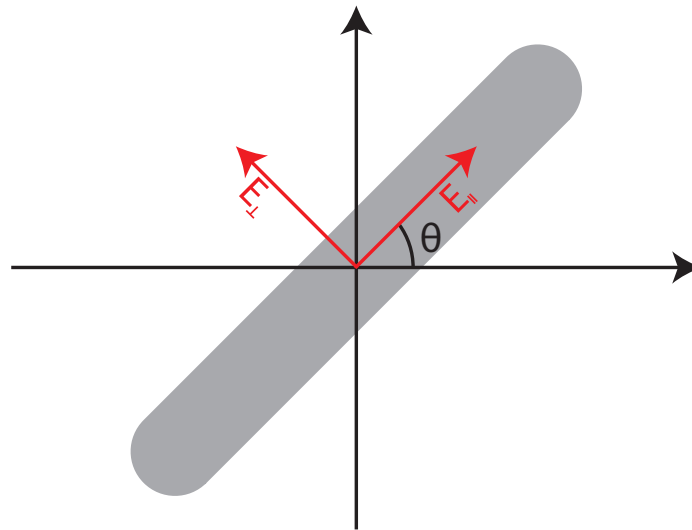


Figure C.1: Particle with components of E-field.

Appendix D

Example Parameter file

```

1  ' ===== Parameter file for v7.3 ====='
   '**** Preliminaries ****'
3  'NOTORQ' = CMDTRQ+6 (DOTORQ, NOTORQ) — either do or skip torque calculations
   'PBCGS2' = CMDSOL+6 (PBCGS2, PBCGST, GPBICG, QMRCCG, PETERKP) — CCG method
5  'GPFAFT' = CMETHD+6 (GPFAFT, FFTMKL) — FFT method
   'GKDLDR' = CALPHA+6 (GKDLDR, LATTD, FLTRCD) — DDA method
7  'NOTBIN' = CBINFLAG (NOTBIN, ORIBIN, ALLBIN) — binary output?
   '**** Initial Memory Allocation ****'
9  100 100 100 = dimensioning allowance for target generation
   '**** Target Geometry and Composition ****'
11 'ELLIPSOID' = CSHAPE+9 shape directive
    49.49 49.49 49.49 = shape parameters 1 – 3
13 1 = NCOMP = number of dielectric materials
    'm1.33_0.01' = file with refractive index 1
15 '**** Additional Nearfield calculation? ****'
    0 = NRFLD (=0 to skip nearfield calc., =1 to calculate nearfield E)
17 0.0 0.0 0.0 0.0 0.0 0.0 (fract. extens. of calc. vol. in -x,+x,-y,+y,-z,+z)
   '**** Error Tolerance ****'
19 1.00e-5 = TOL = MAX ALLOWED (NORM OF |G>=AC|E>-ACA|X>)/(NORM OF AC|E>)
   '**** Maximum number of iterations ****'
21 100 = MXITER
   '**** Integration limiter for PBC calculations ****'
23 1.00e-2 = GAMMA (1e-2 is normal, 3e-3 for greater accuracy)
   '**** Angular resolution for calculation of <cos>, etc. ****'
25 0.5 = ETASCA (number of angles is proportional to [(3+x)/ETASCA]^2 )
   '**** Wavelengths (micron) ****'
27 0.5 0.5 1 'INV' = wavelengths (1st, last ,howmany,how=LIN,INV,LOG,TAB)
   '**** Refractive index of ambient medium ****'
29 1.0000 = NAMBIENT
   '**** Effective Radii (micron) **** '
31 0.39789 0.39789 1 'LIN' = eff. radii (1st, last ,howmany,how=LIN,INV,LOG,TAB)
   '**** Define Incident Polarizations ****'
33 (0,0) (1.,0.) (0.,0.) = Polarization state e01 (k along x axis)
    2 = IORTH (=1 to do only pol. state e01; =2 to also do orth. pol. state)
35 '**** Specify which output files to write ****'
    1 = IWRKSC (=0 to suppress, =1 to write ".sca" file for each target orient.
37 '**** Specify Target Rotations ****'
    0. 0. 1 = BETAMI, BETAMX, NBETA (beta=rotation around a1)
39 0. 0. 1 = THETMI, THETMX, NTHETA (theta=angle between a1 and k)
    0. 0. 1 = PHIMIN, PHIMAX, NPHI (phi=rotation angle of a1 around k)
41 '**** Specify first IWAV, IRAD, IORI (normally 0 0 0) ****'
    0 0 0 = first IWAV, first IRAD, first IORI (0 0 0 to begin fresh)
43 '**** Select Elements of S_ij Matrix to Print ****'
    9 = NSMELTS = number of elements of S_ij to print (not more than 9)
45 11 12 21 22 31 33 44 34 43 = indices ij of elements to print
   '**** Specify Scattered Directions ****'
47 'LFRAME' = CMDFRM (LFRAME, TFRAME for Lab Frame or Target Frame)
    1 = NPLANES = number of scattering planes
49 0. 0. 180. 1 = phi, theta_min, theta_max (deg) for plane A

```

Appendix E

Fortran code added to ddpostprocess.f90

```

1  WRITE(IDVOUT,FMT='(A)') '>DDPOSTPROCESS: executing personal code '
  WRITE(IDVOUT,*) 'NX=',NX
3  WRITE(IDVOUT,*) 'NY=',NY
  WRITE(IDVOUT,*) 'NZ=',NZ
5  WRITE(IDVOUT,*) '>DDPOSTPROCESS: CXEPS=', CXEPS

7  OPEN(UNIT=25,FILE='OPPAR.out', ACTION='write', STATUS='replace')
  WRITE(25,*) NX
9  WRITE(25,*) NY
  WRITE(25,*) NZ
11 CLOSE(25)

13 WRITE(IDVOUT,FMT='(A)') '>DDPOSTPROCESS: processing scattered field '
  OPEN(UNIT=23,FILE='XYZSCA.out', ACTION='write', STATUS='replace')
15 DO JX=1,NX
    DO JY=1,NY
17      DO JZ=1,NZ
        WRITE(23,FMT='(E10.3,5E11.3)') CXESCA(JX,JY,JZ,1),CXESCA(JX,JY,JZ,2),CXESCA(JX,JY,JZ,3)
19      ENDDO
    ENDDO
21 ENDDO
  CLOSE(23)
23

25 WRITE(IDVOUT,FMT='(A)') '>DDPOSTPROCESS: processing incoming field '
  OPEN(UNIT=24,FILE='XYZINC.out', ACTION='write', STATUS='replace')
  DO JX=1,NX
27    DO JY=1,NY
      DO JZ=1,NZ
29        WRITE(24,FMT='(E10.3,5E11.3)') CXEINC(JX,JY,JZ,1),CXEINC(JX,JY,JZ,2),CXEINC(JX,JY,JZ,3)
31        ENDDO
    ENDDO
33 CLOSE(24)

35 WRITE(IDVOUT,FMT='(A)') '>DDPOSTPROCESS: processing location of particle '
  OPEN(UNIT=26,FILE='PART.out', ACTION='write', STATUS='replace')
37 DO JX=1,NX
    DO JY=1,NY
39      DO JZ=1,NZ
        WRITE(26,'(I1)') ICOMP(JX,JY,JZ,1)+ICOMP(JX,JY,JZ,2)+ICOMP(JX,JY,JZ,3)
41        ENDDO
    ENDDO
43 ENDDO
  CLOSE(26)
45

47 WRITE(IDVOUT,FMT='(A)') '>DDPOSTPROCESS: processing polarization '
  OPEN(UNIT=27,FILE='POL.out', ACTION='write', STATUS='replace')
  DO JX=1,NX
49    DO JY=1,NY
      DO JZ=1,NZ
51        WRITE(27,FMT='(E10.3,5E11.3)') CXPOL(JX,JY,JZ,1),CXPOL(JX,JY,JZ,2),CXPOL(JX,JY,JZ,3)

```

```
      ENDDO
53  ENDDO
ENDDO
55  CLOSE(27)

57  WRITE(IDVOUT,FMT='(A)') '>DDPOSTPROCESS: processing polarizability '
OPEN(UNIT=28,FILE='POLBI.out', ACTION='write', STATUS='replace')
59  DO JX=1,NX
      DO JY=1,NY
61      DO JZ=1,NZ
          WRITE(28,FMT='(E10.3,5E11.3)') CXADIA(JX,JY,JZ,1),CXADIA(JX,JY,JZ,2),CXADIA(JX,JY,JZ,3)
63      ENDDO
          ENDDO
65  ENDDO
      CLOSE(28)
67

WRITE(IDVOUT,FMT='(A)') '>DDPOSTPROCESS: processing dielectric function '
69  OPEN(UNIT=29,FILE='EPS.out', ACTION='write', STATUS='replace')
WRITE(29,FMT='(E10.3,E11.3)') CXEPS(1)
71  CLOSE(29)

73  WRITE(IDVOUT,FMT='(A)') '>DDPOSTPROCESS: finished processing personal code.'
```

Appendix F

Importing data

```

1 %% Clearing the workspace
  clear all
3 clc

5 %% Defining variables
  location = '../Software/metingen/ellipsoids_nearfield/g_eps_pr_ar3_phi0_the0/';
7 fileOP = fopen(strcat(location, 'OPPAR.out'));
  filepart = fopen(strcat(location, 'PART.OUT'));
9

11 %% Loading the output periodicities
  OP1 = str2num(fgetl(fileOP)); %Output Periodicity, defines the amount of lines after which it
    will repeat
  OP2 = str2num(fgetl(fileOP));
13 OP3 = str2num(fgetl(fileOP));

15 %% Looping through data files
  for n=0:2
17   %% Scattered field
    filename = strcat('XYZSCA', num2str(n), '.out'); % Define filename
19   file = fopen(strcat(location, filename)); % Open file
    data1 = textscan(file, '%f %f %f %f %f %f', 'CollectOutput', 1) % Scan for lines of specific
      structure
21   mat = data1{1,1}; % Select this data
    Esca = permute(reshape(mat', [6, OP3, OP2, OP1]), [4 3 2 1]); % Cut it into pieces and save it
      to a 4D-array, using the OP's
23   eval(['Esca', num2str(n), '=Esca;']); % Save as numbered variable

25   %% Incoming field
    filenameinc = strcat('XYZINC', num2str(n), '.out');
27   fileinc = fopen(strcat(location, filenameinc));
    data4 = textscan(fileinc, '%f %f %f %f %f %f', 'CollectOutput', 1)
29   mat4 = data4{1,1};
    Einc = permute(reshape(mat4', [6, OP3, OP2, OP1]), [4 3 2 1]);
31   eval(['Einc', num2str(n), '=Einc;']);

33   %% Polarization
    filenameepol = strcat('POL', num2str(n), '.out');
35   filepol = fopen(strcat(location, filenameepol));
    data3 = textscan(filepol, '%f %f %f %f %f %f', 'CollectOutput', 1)
37   mat3 = data3{1,1};
    pol = permute(reshape(mat3', [6, OP3, OP2, OP1]), [4 3 2 1]);
39   eval(['pol', num2str(n), '=pol;']);

41   %% Polarizability
    filenameepolbi = strcat('POLBI', num2str(n), '.out');
43   filepolbi = fopen(strcat(location, filenameepolbi));
    data5 = textscan(filepolbi, '%f %f %f %f %f %f', 'CollectOutput', 1)
45   mat5 = data5{1,1};
    polbi = permute(reshape(mat5', [6, OP3, OP2, OP1]), [4 3 2 1]);
47   eval(['polbi', num2str(n), '=polbi;']);

49   %% Dielectric function
    filenameeeeps = strcat('EPS', num2str(n), '.out');
51   fileeps = fopen(strcat(location, filenameeeeps));

```

```
53     Epst = str2num(fgetl(fileeps));
54     Eps(n+1) = Epst(1)+i*Epst(2);
55 end
56 %% Target composition
57 data2 = textscan(filepart, '%f', 'CollectOutput', 1)
58 mat2 = data2{1,1};
59 part = permute(reshape(mat2', [OP3, OP2, OP1]), [3 2 1]);
60 fclose all;
61 %% Saving the data
62 clearvars Esca Einc pol polbi
63 save(strcat(location, 'data3D.mat'), 'Esca*', 'Einc*', 'OP*', 'part', 'pol*', 'Eps', 'polbi*');
```

Appendix G

Processing the fields

```

%% Clearing workspace
2 clearvars -except Esca* OP* part Einc* pol* Eps polbi*
  clc
4 close all

6 %% load data
% load( '../Software/metingen/cylcap_nearfield/g_cylcap_ar7_octupiek_phi45/Data3D.mat' );
8

%% Definitions
10 pos = round(OP3/2); % Position of the 2D cross section
  step = 10; % Step size of the vectorplots
12 vlak = 'XZ'; % Cross section to be examined

14 %% Loop through the different images
for im = 0:2
16   %% Selecting the right data
    eval(['Etot = Esca',num2str(im),' + Einc',num2str(im),'']); % Calculating total field
18   eval(['P = pol',num2str(im),'']); % Selecting the right polarization
    eval(['alpha = polbi',num2str(im),'']); % Selecting the right polarizability
20   Etoti(:,:,1:3) = Etot(:,:,:,1:2:5)+i*Etot(:,:,:,2:2:6); % Expressing the E-field in
    complex numbers
    alphi(:,:,:,1:3) = alpha(:,:,:,1:2:5)+i*alpha(:,:,:,2:2:6); % Expressing the polarizability
    in complex numbers
22   Pi(:,:,:,1:3) = P(:,:,:,1:2:5)+i*P(:,:,:,2:2:6); % Expressing the polarization in complex
    numbers
    corr = part/3 * ((Eps(im+1)+2)/3) + (1-part/3); % Creating the conversion matrix from Emac
    to Emic
24   corr = repmat(corr,[1,1,1,3]); % Creating the conversion matrix from Emac to Emic
    Eloci = Etoti .* corr; % Calculating the local field
26

    %% Calculate charge distribution
28   Etotkm = permute(Etot,[2 1 3 4]); % Flipping X and Y dimension because Matlab sucks arse
    [XX,YY,ZZ] = meshgrid(1:OP1,1:OP2,1:OP3); % Creating meshgrid for the E-field
30   div3Dkm = divergence(XX,YY,ZZ,Etotkm(:,:,:,1),Etotkm(:,:,:,3),Etotkm(:,:,:,5))./(4*pi); %
    Calculating divergence of Re(E-field) in 3 dimensions
    div3D = permute(div3Dkm,[2 1 3]); % Flipping X and Y dimension back for human readability
32

    %% Calculate dipole moment
34   % As a check, the dipole moment will be calculated in two ways. This
    % way, we can check if no errors are made in the code.
36   % The first method to calculate the dipole moment is by summing the
    % polatzation field, in order to obtain the total dipole moment. This
38   % is done in the next line.
    sumP(im+1,1:3) = [sum(sum(sum(P(:,:,:,1)))) sum(sum(sum(P(:,:,:,3)))) sum(sum(sum(P
    (:,:,:,5)))))]; % Summing over the polarization field in every direction to obtain the
    total dipole moment
40   % The second method to calculate the dipole moment is by taking the
    % charge distribution and multiplying every point with its distant to
42   % the origin. The point (x,y,z)=(0,0,0) is chosen as origin, but since
    % the total charge is zero, this can be any point. The total dipole
44   % moment is independent of the origin.
    dipmomkm = cat(4,div3Dkm.*XX, div3Dkm.*YY, div3Dkm.*ZZ); % Multiplying the charge with its
    distance (index)
46   dipmom = permute(dipmomkm,[2 1 3 4]); % Swapping the X and Y dimensions again

```

```

sumPP(im+1,1:3) = [sum(sum(sum(dipmom(:,:,1)))) sum(sum(sum(dipmom(:,:,2)))) sum(sum(
    sum(dipmom(:,:,3))))]; % Summing over the polarization field in every direction to
    obtain the total dipole moment
48
%% Choosing correct cross-section
50 if strcmp(vlak, 'XY')
    E = permute(Etot(:,:,pos,:), [1 2 4 3]); % Defining 2D cross section of E-field
52    div2D = div3D(:,:,pos); % Defining 2D cross section of charge distribution
    partcs = part(:,:,pos); % Defining 2D cross section of particle
54    grens = edge(part(:,:,pos)); % Calculating the edge of the particle in 2D
    polt = permute(P(:,:,pos,:), [1 2 4 3]); % Defining 2D cross section of polarization
56    A = 1; % Defining the right index
    B = 3; % Defining the right index
58    temp1=1:step:OP1; % Defining spacing grid for vectorplot
    temp2=1:step:OP2; % Defining spacing grid for vectorplot
60 elseif strcmp(vlak, 'YZ')
    E=permute(Etot(pos,:,:,:), [2 3 4 1]);
62    div2D = permute(div3D(pos,:,:,:), [2 3 1]);
    partcs = permute(part(pos,:,:,:), [2 3 1]);
64    grens = edge(permute(part(pos,:,:,:), [2 3 1]));
    polt = permute(P(pos,:,:,:), [2 3 4 1]);
66    A = 3;
    B = 5;
68    temp1=1:step:OP2;
    temp2=1:step:OP3;
70 elseif strcmp(vlak, 'XZ')
    E=permute(Etot(:,pos,:,:), [1 3 4 2]);
72    div2D = permute(div3D(:,pos,:), [1 3 2]);
    partcs = permute(part(:,pos,:), [1 3 2]);
74    grens = edge(permute(part(:,pos,:), [1 3 2]));
    polt = permute(P(:,pos,:,:), [1 3 4 2]);
76    A = 1;
    B = 5;
78    temp1=1:step:OP1;
    temp2=1:step:OP3;
80 end

82 %% Drawing the particle
figure
84 [X, Y] = find(grens);
    scatter(X,Y, 'red', '.');
86 hold on
axis equal
88 asfix(vlak, OP1, OP2, OP3)

90 %% Plot vector field
[x, y]=meshgrid(temp2, temp1);
92 quiver(y, x, E(temp1, temp2, A), E(temp1, temp2, B), 'black');

94 %% Generating streamlines
for n = 1:3:length(X)
96    Xs = X(n)+sign(X(n)-round(size(E,1)/2));
    Ys = Y(n)+sign(Y(n)-round(size(E,2)/2));
98    streamline(E(:,:,A), E(:,:,B), Xs, Ys);
    streamline(-E(:,:,A), -E(:,:,B), Xs, Ys);
100 end
title(['Electric field lines'])
102 xlabel(['x-axis (nm)'])
ylabel(['y-axis (nm)'])
104 name1 = strcat('quadfield', num2str(im));
    % processcharge(100,30,name1)
106 % saveas(gcf, fullfile('C:\Users\Kit\Desktop\Bachelor opdracht\Report\Images', name1),
    'epsc')

108 %% Plot charge distribution
figure
110 imagesc(div2D', [-0.4 0.4])
hold on
112 axis equal
    asfix(vlak, OP1, OP2, OP3)
114 set(gca, 'YDir', 'normal')
title('Charge distribution and dipole moment')
116 xlabel('x-axis (nm)')

```

```

118     ylabel('y-axis (nm)')
name2 = strcat('quadcharge', num2str(im));
% processcharge(100,30,name2)
120     qh = quiver(size(E,1)/2, size(E,2)/2, sumP(im+1, (A+1)/2), sumP(im+1, (B+1)/2), 0.005, 'red'); %
        Plot dipole moment
        set(qh, 'LineWidth', 3);
122     % saveas(gcf, fullfile('C:\Users\Kit\Desktop\Bachelor opdracht\Report\Images', name2),
        'eps')

124     %% Convergence check
P2i = 1./alphi.*Eloci; % Calculate P from E and alpha, where the alphi array actually
        consists of 1/alpha
126     P2i(abs(P2i(:))==Inf | isnan(abs(P2i(:)))) = 0; % Since alphi is inverted and equal to
        zero outside the particle, outside the target P2i will be Inf (or NaN), this is
        corrected with this line.
P2(:,:,,1:2:5) = real(P2i(:,:,,1:3)); % Convert the complex numbers back to real numbers
128     P2(:,:,,2:2:6) = imag(P2i(:,:,,1:3)); % Convert the complex numbers back to real numbers
Pdiff(im+1) = sum(abs(P2(:) - P(:)))/numel(find(part==3)); % Calculate the average
        deviation
130 end

132 %% Display the checks
Perr = sumP./sumPP;
134 disp(sprintf(strcat('The relative difference between the two dipole moment calculations is:\n'
        , 'Px\t\t\t Py\t\t\t Pz\n', num2str(mean(Perr)), '\n')))
disp(sprintf(strcat('The average error in the convergence is:\n', num2str(mean(Pdiff)))))
136

138 %% Unused
% qh = quiver(size(E,1)/2, size(E,2)/2, sumP(im+1, (A+1)/2), sumP(im+1, (B+1)/2), 0.0005, 'red');
% Plot dipole moment
140 % set(qh, 'LineWidth', 3);
% qh2 = quiver(size(E,1)/2, size(E,2)/2, sumPP(im+1, (A+1)/2), sumPP(im+1, (B+1)/2), 0.0005, '
blue'); % Plot dipole moment
142 % set(qh2, 'LineWidth', 1);
% quiver(y,x, permute(Einc0(temp1, temp2, pos, A), [1 2 4 3]), permute(Einc0(temp1, temp2, pos, B)
, [1 2 4 3]), 'black');
144
% dipmom2km = cat(4, div3Dkm.*(XX-OP2/2), div3Dkm.*(YY-OP1/2), div3Dkm.*(ZZ-OP3/2));
146 % dipmom2 = permute(dipmom2km, [2 1 3 4]);

148 % Gam = cross(dipmom2, real(Eloci), 4);
% gamtot(im+1, 1:3)=sum(sum(sum(Gam)));
150
% Eloc(:,:,,1:2:5) = real(Eloci(:,:,,1:3));
152 % Eloc(:,:,,2:2:6) = imag(Eloci(:,:,,1:3));
% Etot = Eloc;

```